Development of Nanofocusing Refractive X-Ray Lenses

Von der Fakultät für Mathematik, Informatik und Naturwissenschaften
der Rheinisch-Westfälischen Technischen Hochschule Aachen zur
Erlangung des akademischen Grades einer Doktorin der
Naturwissenschaften genehmigte Dissertation

vorgelegt von

Diplom-Physikerin Olga Kurapova
aus Taschkent

Berichter: Professor B. Lengeler
Professor U. Klemradt

Tag der mündlichen Prüfung: 02.11.2005

Table of contents

Chapter 1

Introduction

1.1 Scientific background

Large penetration depth in matter and small wavelengths make hard x–rays attractive for microanalysis, such as x-ray diffraction, fluorescence analysis, and absorption spectroscopy. These methods are powerful tools in semiconductor technology, in material science, geology, biology, or medicine, and are particularly useful for investigating non-destructively structures inside a specimen. To perform x-ray analysis techniques with spatial resolution well below 100 nm, synchrotron radiation from a third generation source with its outstanding properties, such as brilliance and flux, and high quality optical components are needed. For focusing purposes in the micrometer and sub-micrometer range highly sophisticated components like Kirkpatrick – Baez mirrors [**Kirk**], [**Haya**], [**Hign1**], Fresnel zone plates [**Yun**] and refractive x-ray lenses [**Len1**], [**Aris**], [**Schr1**] have been developed in the last years.

The typical synchrotron radiation source size is a few hundred μm (e.g., European Synchrotron Radiation Facility (ESRF), high-β undulator source size: 900×60 μm^2, low-β undulator source 150×60 μm^2). To achieve a microbeam size in the 100 nm range a demagnification by a factor of 1000 is required. At a typical distance of 40-70 m from the radiation source most x-ray optics with a focal distance larger than

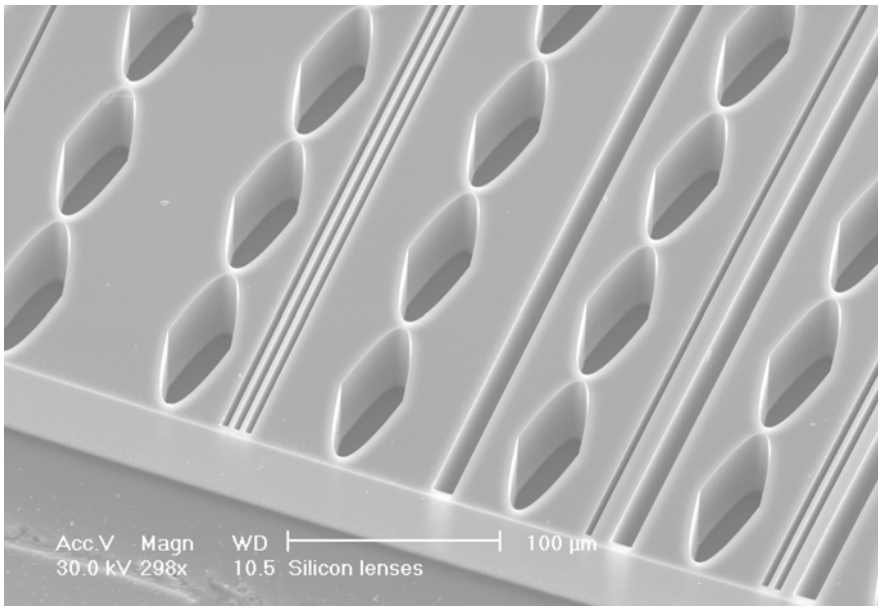

Figure 1.1. Scanning electron micrograph of planar parabolic refractive nanofocusing lenses made of silicon.

10 cm can not reach this demagnification. One possibility to reach this limit (100 nm) is making a smaller secondary source by placing a pinhole between source and microbeam setup [**Yun**]. Another possibility is to place the microprobe at a large distance from the source, e.g. at 145 m [**Hign1**] or 1 km [**Yam**], if this space is available. At Aachen University a third alternative was pursued. Nanofocusing refractive lenses (NFLs) were developed with focal distance f of a few mm [**Schr1**] that allows for demagnification of several thousand even at short beamlines. This small focal distance and strong demagnification can only be realised with a lens curvature R in the range of few µm. Because fabrication techniques for rotationally parabolic refractive lenses developed at Aachen University [**Len1**] are not well suited to fabricate such strongly curved lenses, a new microfabrication process for the lenses

with a cylindrically parabolic profile and extremely small R is required. For this purpose, a lithographic techniques such as electron beam lithography combined with deep reactive ion etching was used. Silicon nanofocusing refractive lenses are made by etching a series of parabolic cylinders into the lens material (**Figure 1.1**). These one-dimensionally focusing lenses require vertical sidewalls to be generated in the etching process. Deviations from the ideal shape lead to aberrations and thus to a blurred focus. Using nanofocusing refractive x-ray lenses, a nanobeam with a lateral resolution of 50 nm has been generated [**Schr2**], that is in good agreement with the calculated value for ideal lenses.

1.2 Objectives

In this work the microfabrication process of nanofocusing x-ray refractive lenses made by lithographic techniques has been investigated. The goal was to contribute towards understanding the etching process, lens shape, and focus properties.
This thesis is concerned with:

- the optimisation of the fabrication process for nanofocusing x-ray lenses made of silicon;
- characterization of the silicon NFLs;
- application of the NFLs;
- microfabrication processes for nanofocusing x-ray lenses made of boron, diamond, graphite, and sapphire.

For the microfabrication process electron beam evaporation and electron beam lithography were used. Different methods of etching, such as wet etching, reactive ion etching, and deep reactive ion etching were applied. Analytic techniques for the

determination of lens shapes were scanning electron microscopy (SEM), optical microscopy (OM), profilometer (MicroProf®). The lenses were tested at the low-β beamline ID13 of ESRF.

1.3 Research strategy

X-ray optics development is often motivated by the application potential. In this work a research strategy is adopted which is based on the close dependence of the microfabrication process with the lenses shape, properties (focus size) and application of the nanofocusing x-ray lenses (**Figure 1.2**).

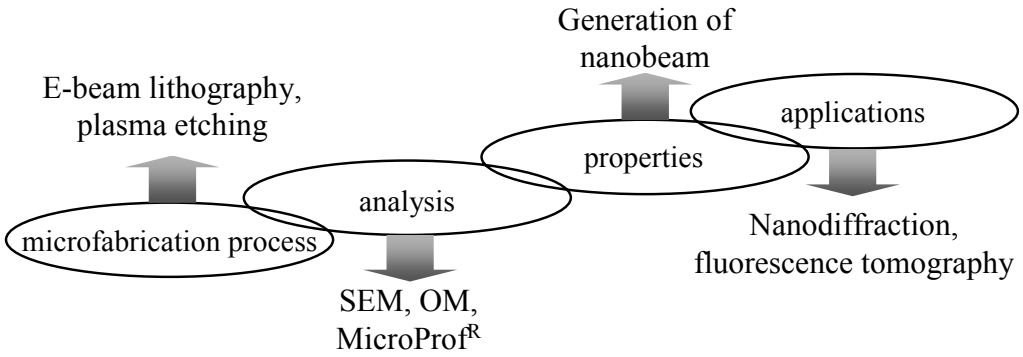

Figure 1.2. Research strategy.

During e-beam lithography and plasma etching, the analysis of parameters, such as exposure time, exposure doses, exposure energies and gas inflow, gas mixture, pressure, rf power is employed to gain understanding of the correlation between microfabrication conditions and the lens shape evolution. *Ex-situ* techniques (SEM,

OM, MicroProf®) are used for the lens shape analysis as well as for the characterization of the radius of curvature. Nanofocusing refractive lenses with lens shapes close to optimal (parabolic shape and vertical sidewalls) are employed to generate monochromatic hard x-ray beams well below 100 nm. Based on these lenses, microanalysis in the range of 100 nm and below, such as x-ray diffraction, fluorescence analysis, and absorption spectroscopy can be successful carried out.

Chapter 2

Theoretical background

2.1 Refractive optics

2.1.1 Absorption

When x-rays pass through matter, they are attenuated. This behaviour is described by Lambert-Beer's law:

$$I(x) = I_0 e^{-\mu x}. \tag{2.1}$$

Here, I_0 is the intensity before the sample, and $I(x)$ is the remaining intensity after a homogeneous slice of material of the thickness x.

The linear absorption coefficient μ (**Figure 2.1**) contains contributions from photoabsorption τ, elastic scattering σ_R (Raleigh scattering), inelastic scattering σ_C (Compton scattering), and pair production σ_{pair} for x-rays above 1,022 MeV.

$$\mu = \tau + \sigma_R + \sigma_C (+\sigma_{pair}). \tag{2.2}$$

Values for the mass absorption coefficient μ/ρ, where ρ is the density, can be found in the literature for almost all elements and for a wide range of x-ray energies [**Veig**]. For compound materials, the mass absorption coefficient of the elements are weighted with the relative density

$$\rho_i = \rho \frac{\nu_i A_i}{\sum_j \nu_j A_j}, \tag{2.3}$$

where ν_i is the number of atoms and A_i the atomic weight of the component *i*. Thus, the linear absorption coefficient of a compound is

$$\mu = \sum_i \left(\frac{\mu}{\rho} \right)_i \rho_i . \tag{2.4}$$

The absorption coefficient changes with the photon energy. In general, the attenuation decreases with increasing energy. However, at the binding energies of the electrons a jump a so-called absorption edge, appears due to the onset of photoabsorption of the respective atomic shell (**Figure 2.1**).

In the absorption process, an electron is released from the atom as photoelectron (**Figure 2.2a**). Photoabsorption is strongest for tightly bound inner electrons. On the other hand, absorption by the outer shell electrons is weak, since they are not bound strongly enough to the nucleus for it to easilyy take up the surplus momentum of the photon. The kinetic energy of the photoelectron is the difference between the incident photon energy and the binding energy of the atom's shell.

The hole in the inner shell is then filled by an electron from an outer shell. The surplus energy of this process is either transferred to a fluorescence photon (**Figure 2.2b**) or to an Auger electron (**Figure 2.2c**). The probability of the two competing processes depends on the element in which it occurs. **Figure 2.3** shows the yield for the K_α fluorescence versus the atomic number *Z*. The fluorescence yield increases with increasing atomic number, while the yield for Auger electrons decreases accordingly.

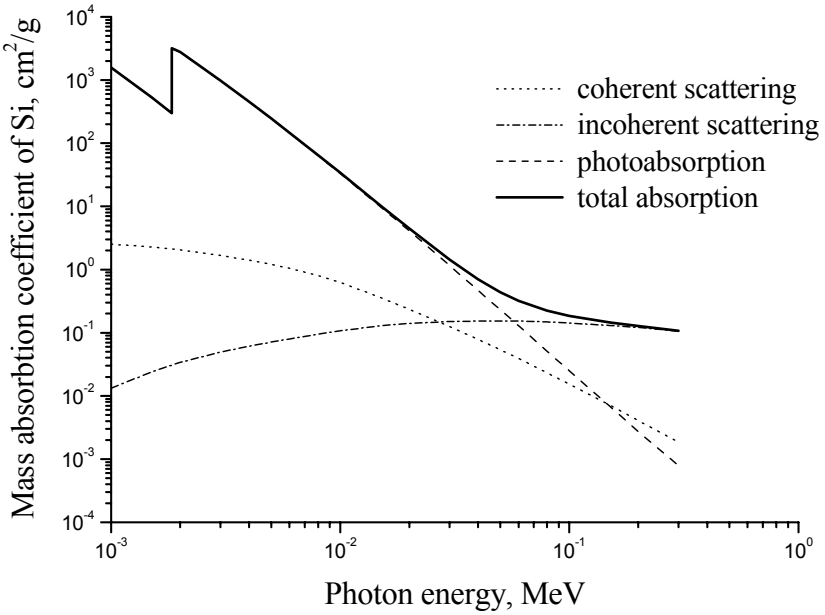

Figure 2.1. The total mass absorption coefficient for silicon [**Berg**].

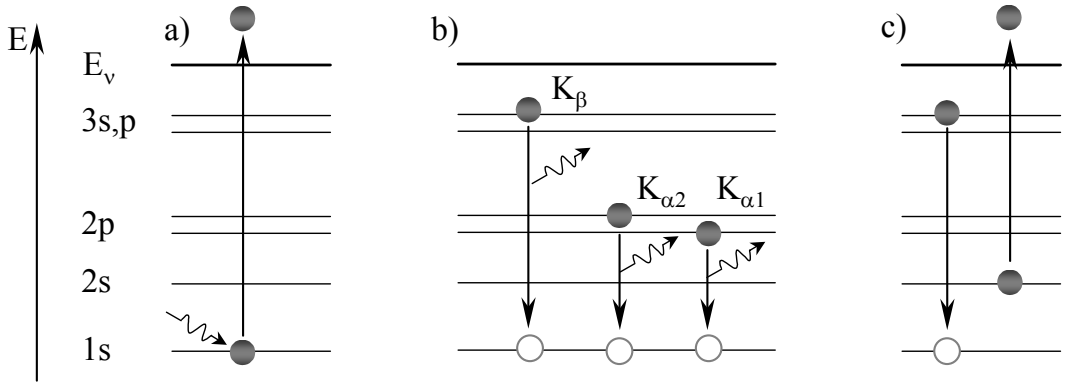

Figure 2.2. X-ray absorption with the creation of a) a photoelectron and the two possible secondary processes: b) fluorescence and c) emission of an Auger electron.

2.1.2 Refractive index

The refractive index for x-rays can be written as [**Jam**]

$$n = 1 - \delta + i\beta, \tag{2.5}$$

where δ describes the refraction; the imaginary part β describes the absorption and is connected to the photoabsorption τ via $\tau = \frac{4\pi}{\lambda}\beta$, where λ is the wavelength of the photons.

Both δ and β can be calculated from the atomic scattering factor $f(\vec{K} = 0) = Z + f' + if''$ in the forward direction, where Z is the atomic number and $f'+if''$ is the dispersion correction:

$$\delta = C(Z + f'), \tag{2.6}$$

$$\beta = Cf'', \tag{2.7}$$

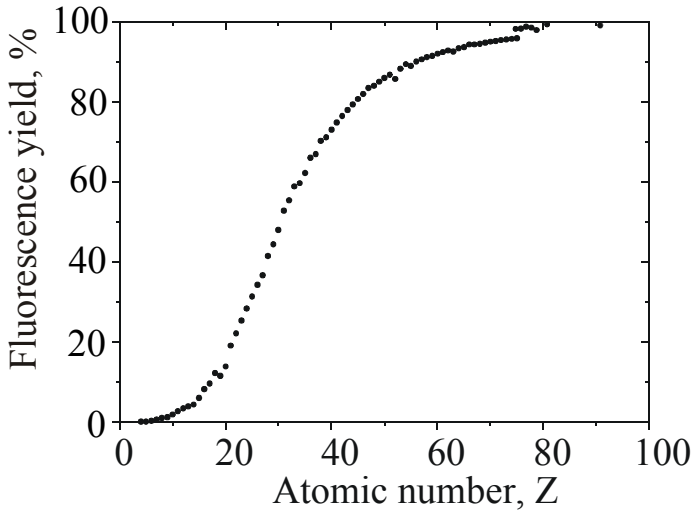

Figure 2.3. Fluorescence yield for the K_α-line versus the atomic number Z [**Grig**].

$$C = \frac{N_a}{2\pi} r_0 \lambda^2 \rho \frac{1}{A} . \tag{2.8}$$

For compound materials, δ and β are also calculated in analogy to the relative density (**Equation 2.4**). Thus, δ can be written as

$$\delta = \sum_i \frac{N_a r_0 \lambda^2}{2\pi} \frac{Z_i}{A_i} \rho_i = \frac{N_a r_0 \lambda^2 \rho}{2\pi} \frac{\sum_i \nu_i Z_i}{\sum_j \nu_j A_j} , \tag{2.9}$$

away from the absorption edges. Similarly, β or τ can be written as

$$\tau = \frac{4\pi}{\lambda} \beta = \frac{4\pi}{\lambda} \sum_i \frac{N_a r_0 \lambda^2}{2\pi} \frac{f_i''}{A_i} \rho_i = \sum_i \left(\frac{\tau}{\rho} \right)_i \rho_i . \tag{2.10}$$

The refractive index for x-rays deviates only very little from unity, since both δ and β are very small. δ is of the order of 10^{-6} for most materials at photon energies around 10 keV; β is even smaller by two or three orders of magnitude. Hence, the refraction is only very small. Since δ is positive, the real part of the refractive index n is smaller than unit. Thus, according to Snell's law [**Hech**]

$$n_1 \cos(\theta_1) = n_2 \cos(\theta_2) , \tag{2.11}$$

the x-rays that pass from vacuum (or air) into matter are refracted away from the surface normal (**Figure 2.4b**). For visible light, the refraction is towards the surface normal (**Figure 2.4a**), since n_2 is larger than 1.

For the angle θ_1 in **figure 2.4b**, which is smaller than a certain critical angle θ_c, the x-rays are totally reflected from the sample surface. According to **equation 2.11**, the critical angle θ_c can be calculated from

$$\cos(\theta_c) = n_2 \quad \rightarrow \quad 1 - \frac{\theta_c^2}{2} \cong 1 - \delta \quad \rightarrow \quad \theta_c \cong \sqrt{2\delta} . \tag{2.12}$$

Above the critical angle θ_c, a part of the radiation is transmitted. For increasing angles θ_1, the part of the incoming x-rays that is reflected diminishes rapidly. Due to this external total reflection, a mirror for x-rays works in grazing incidence. As δ decreases with increasing energy, the reflection can serve as a low-pass filter.

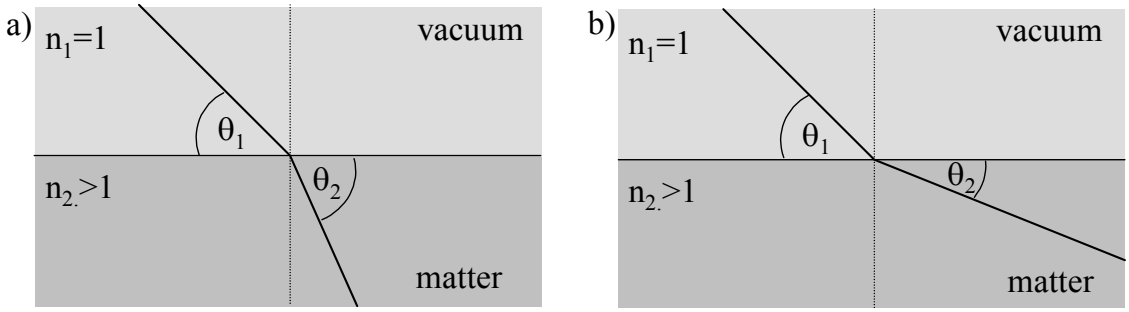

Figure 2.4. Refraction for a) visible light and for b) x-rays.

2.1.3 Focusing optics for hard x-rays

Like for conventional optics in the visible light range one can use reflection (focusing mirrors), refraction (refractive lenses), and diffraction (diffractive lenses, zone plates) in order to deflect and therefore focus light. However, there are some peculiarities originating from the fact, that for x-rays the real part of the refractive index is typically very close to unity and the same time the imaginary part (describing absorption) comparatively large.

X-ray mirror optics take advantage of the fact that the refractive index of all materials in the x-ray range is smaller than one so that total reflection can be achieved if light falls unto a sufficiently flat surface. As the real part of the refractive index is very

close to unity, a grazing incidence of the x-rays, almost parallel to the mirror surface, is required in order to obtain total reflection. Due to these small working angles x-ray mirrors are relatively hard to align and often suffer from strong aberrations. In addition very long mirrors with high shape accuracy are required making high performance mirror systems difficult to build and comparatively expensive. In consequence, a spot size of about 1 μm can be obtained in routine operation, although spot-sizes down to 100 nm FWHM have been reported recently [**Hign2**], [**Cloe**], [**Ice**]. As x-ray mirrors have the advantage of being achromatic and show comparatively high efficiency, they are quite often used as x-ray focusing devices.

Refractive lenses for x-rays are a relatively new development and in fact have been considered impractical for a long time due to the small refraction effects and the strong absorption of materials in the x-ray range. Nevertheless, using many lenses in series it is possible to obtain a sufficient deflection of the beam, and therefore reasonable focal lengths [**Snig**]. And going to high photon energies, using lens materials with low atomic number and utilizing alternative approaches for the lens fabrication and design [**Len2**], [**Aris**] it is possible to keep absorption losses small. Refractive lenses for x-rays are strongly chromatic – the focal length is found to be proportional to the square of the used photon energy. However, many applications require monochromatized x-rays of a fixed energy, so that chromatic aberrations are normally negligible and do not significantly limit the applicability of refractive lenses. A short overview of microfocusing theory for different types of refractive x-ray lenses can be found below.

Diffractive lenses (zone plates) for x-rays offer the advantage that the diffractive structures together with the support membrane can be kept very thin, so that even for soft x-rays, where absorption plays a dominant role, a sufficiently high x-ray transmission can be realized. The diffractive structures can be fabricated with high

accuracy down to very small structure sizes and as a consequence zone plates achieve by far the highest resolution of all x-ray lenses [**Schn**], [**Spec**], [**And**], [**Dav**]. Similar to refractive lenses diffractive x-ray lenses have the disadvantage of being chromatic – the focal length is directly proportional to the photon energy. Another drawback of diffractive lenses is, that it is very difficult to obtain sufficient diffraction efficiency in the hard x-ray range. This results from the fact, that good efficiencies require structure heights, which are often much larger than the periods of the diffracting structures, making the fabrication of zone plates with the demanded aspect ratios a non-trivial task.

There are also many other alternative methods to achieve a small spot of x-rays, like Bragg-Fresnel lenses, capillary optics and wave-guides. Consequently, many books and several reviews can be found in the literature, discussing in the detail the advantages and disadvantages of all these methods and the fields of their application (see for example [**Mich**]).

2.1.4 Refractive x-ray lenses

The first refractive lenses for hard x-rays were reported in 1996 [**Snig**]. The lenses were drilled holes (**Figure 2.5a**), with a radius of 300 μm, in bulk aluminium with cylindrical or cross-cylindrical geometry. At 14 keV a spot size of 8 μm was measured. For these lenses spherical aberrations take place. To avoid artefacts and distortions in the imaging, the x-ray lens shape has to be parabolic (**Figure 2.5b**). Experiments with stacked parabolic refractive lenses made of aluminium were presented in 1999 [**Len1**]. The imaging abilities were demonstrated

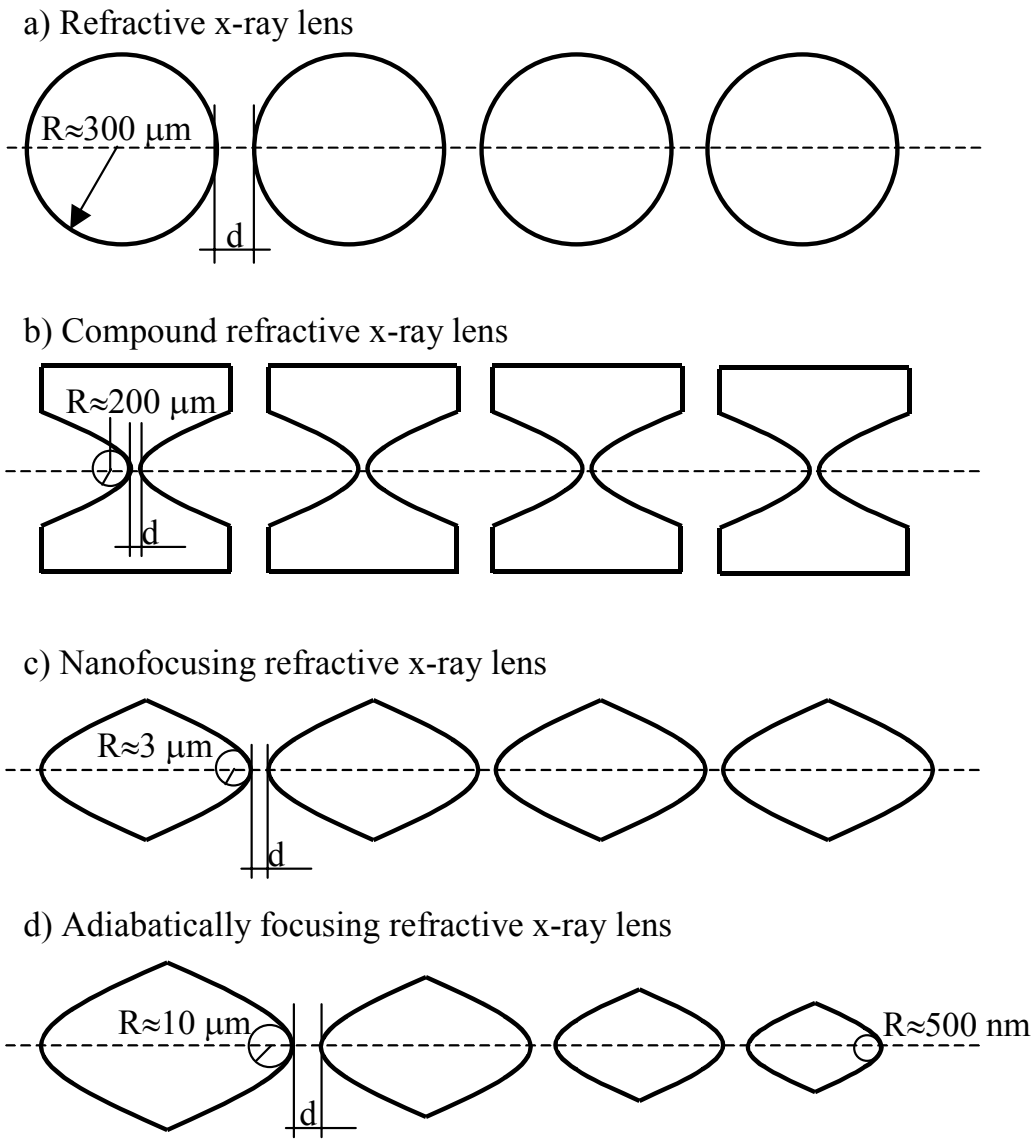

Figure 2.5. Sketch of types of parabolic refractive lenses: a) first refractive lenses; b) compound refractive x-ray lenses; c) nanofocusing refractive x-ray lenses; d) adiabatically focusing refractive x-ray lens.

with crossed gold meshes. Later, tomographic and microprobing application were implemented. Beryllium parabolic refractive lenses were first manufactured in 2001. The typical radius of curvature of these lenses is about 200 μm. For the focusing in the range of 100 nm and below, nanofocusing refractive lenses with crossed parabolic cylinder symmetry were developed (**Figure 2.5.c**). The first publication about nanofocusing refractive x-ray lens made of silicon can be found in [**Schr1**]. The most outstanding feature of these lenses is their small radius of curvature R, that lies in the micrometer range and leads to focal distances in the centimetre range for hard x-rays. The concept of special refractive lenses for focusing in range of few nanometers has been a new approach since 2005 [**Schr2**]. The principal difference between nanofocusing refractive lenses and adiabatically refractive lenses is in the fact, that the second have continuously decreasing radius of curvature (**Figure 2.5d**). The properties of compound refractive x-ray lenses have in details been described in [**Schr3**]. Characteristic properties of adiabatically focusing refractive lenses are given in **section 2.10.**

2.1.5 Focal length

The refraction of x-rays in matter has already been discussed above. On this basis, refractive lenses for x-rays can be constructed in an analogous manner to the well-known glass lenses for visible light. The focal length for both cases can be described by the lens maker's formula

$$\frac{1}{f} = \frac{2(n-1)}{R}, \tag{2.13}$$

where n is the real part of the refractive index and R is the radius of curvature of the lens. However, some differences have to be noticed.

First, the refractive index for x-rays in matter is < 1, as can be seen from **equation 2.5**. Thus, a focusing lens has to be concave for x-rays, while it is convex for visible light.

Second, since δ in **equation 2.5** is very small, the refractive index is close to 1. Thus, as can be seen from **equation 2.13**, the radius of curvature of an x-ray lens has to be very small to achieve a manageable focal length. To reduce the focal length of nanofocusing x-ray refractive lenses to a few millimetres, a radius of curvature in the range of several micrometers is required. Moreover, the focal length can be reduced by using a set of lenses with the individual focal lengths f_i. The system of several lenses can be realized by etching single lenses behind each other into the lens material. As long as the focal length of such a system is still long compared to the thickness of the stack, the system can be treated as a thin lens and the focal length can be calculated as

$$\frac{1}{f} = \sum_i \frac{1}{f_i}. \tag{2.14}$$

Thus, for N identical lenses, where each has two surfaces with radius of curvature R, the focal length is

$$f_0 = \frac{R}{2N\delta}, \tag{2.15}$$

where δ is the refractive index decrement (**Equation 2.5**).

If the total length of the lens has comparable size to the focal length (**Figure 2.6**), then the thin lens approximation is no longer valid. The correction to f has been calculated [**Schr3**]. It turns out that for thick lenses f is given by

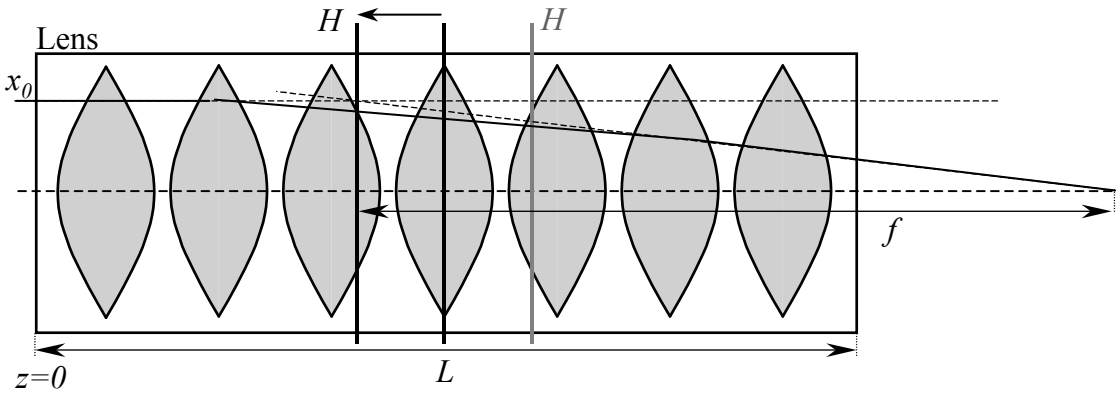

Figure 2.6. The focal length and the principal planes of a thick refractive lens.

$$f = Lx\frac{1}{\sin x}. \tag{2.16}$$

Here, $x = \sqrt{\frac{f_0}{L}}$, L is the total length of the stack. The focal length f is measured from the principal plane H (**Figure 2.6**) with

$$H = L\left(\frac{1}{2} - x\frac{1-\cos x}{\sin x}\right). \tag{2.17}$$

Third, the absorption of x-rays is significant in all materials. To reduce attenuation in the lens to a minimum, materials with a low atomic number Z are necessary [**Len3**]. Further criteria for the choice of the lens material are its machinability, a low small angle scattering and its stability in an x-ray beam of high energy and intensity.

2.1.6 Generation of a small focal spot

Note that the nanofocusing refractive x-ray lenses are not suitable for the imaging due to crossed geometry and can be used mainly for the generation of a small focal spot.

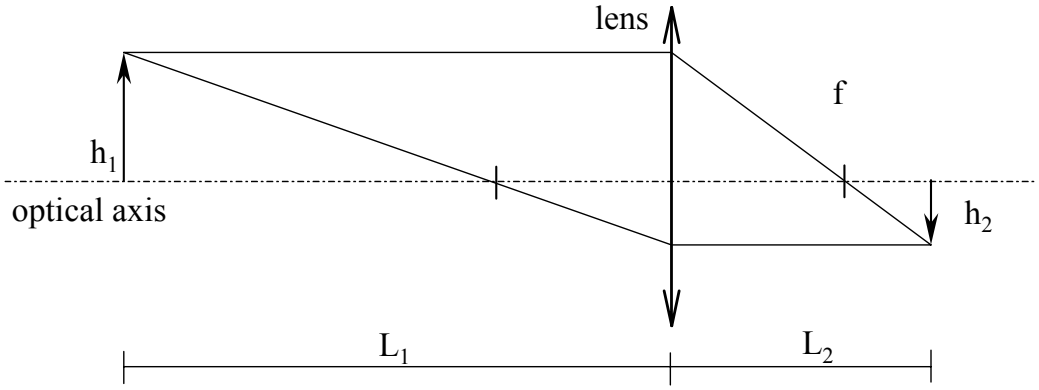

Figure 2.7. Generation of a small focal spot. For nanofocusing refractive lenses: $L_2 \approx f$.

The demagnification factor can be written as

$$m = \frac{f}{L_1 - f}, \tag{2.18}$$

where f is focal distance, L_1 the distance between source and lenses, (**Figure 2.7**). The demagnification of the source in the range of several thousand can be obtained.

2.1.7 Effective aperture

The aperture of a glass lens for visible light is only limited by its size, since almost no light is absorbed in the lens. However, the absorption of x-rays in matter can not be neglected, and thus, the transmission of an x-ray lens decreases for rays away from the optical axis, since it is concave and the thickness of the lens material that these rays have to pass through increases rapidly due to the very small radius of curvature.

For refractive x-ray lenses with N single lenses, the effective aperture can be written as

$$D_{eff} = 2\sqrt{\frac{2R}{\mu N}}, \tag{2.19}$$

provided that the geometric aperture is so large that the attenuation of the lens material dominates D_{eff}. Here, R is the radius of curvature of the parabola, and μ is linear absorption coefficient of the lens material.

2.1.8 Numerical aperture

Connected with the effective aperture D_{eff} is the concept of the numerical aperture *N.A.*. Photons that come from an object can only contribute to an image, if they pass through the effective aperture D_{eff} of the lens. As can be seen from **figure 2.8** there is a maximum effective angle α that rays coming from the object at L_1 can have with the optical axis, so that they can still pass through the effective aperture of the lens. Rays with a larger angle would most likely be absorbed in the lens material. The numerical aperture *N.A.* is defined as the sine of that maximum effective angle and can be written for small angles α as

$$N.A. = \sin\alpha \approx \frac{D_{eff}}{2L_1}. \tag{2.20}$$

2.1.9 Diffraction limit

In addition to the demagnification of the source, the microbeam can also be limted by diffraction at the aperture of the lens. As described above the effective aperture is dominated by attenuation in the outer parts of the lens for most lenses with short focal

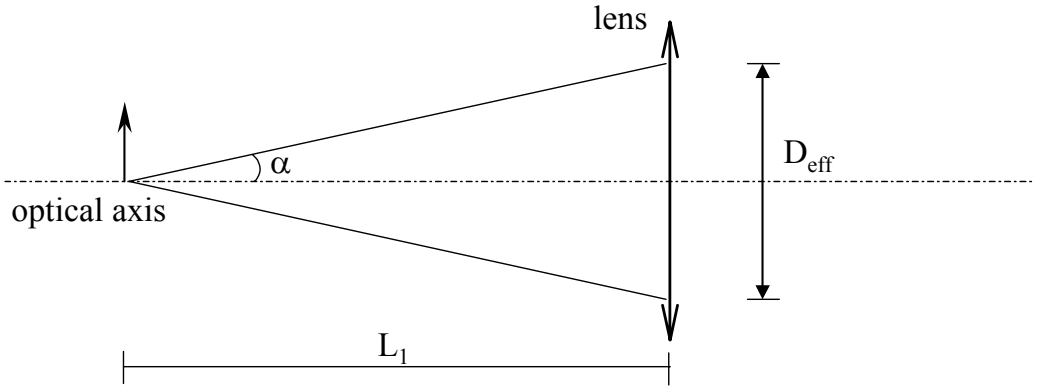

Figure 2.8. Definition of the numerical aperture of a lens.

distance. The aperture of the lens is nearly Gaussian, giving rise to a Gaussian-Airy disc. Using the full width at half maximum of the Airy disc, the transverse resolution of the optical system can be defined. It is given by

$$d_t = \frac{2\sqrt{2\ln 2}}{\pi}\frac{L_1}{D_{eff}}\lambda = \frac{2\sqrt{2\ln 2}}{\pi}\frac{1}{2N.A.}\lambda \approx 0.75\frac{\lambda}{2N.A.} \qquad (2.21)$$

where λ is the wave length of the x-rays and $N.A.$ is numerical aperture.

Figure 2.9 shows the optimal diffraction limit that can be obtained with nanofocusing refractive lenses made of different materials.

2.1.10 Adiabatically focusing lenses

The minimal spot size achievable with nanofocusing refractive lenses lies below 20 nm and is limited by the constant refractive power per unit length inside the NFL constant aperture. Schroer and Lengeler [**Schr2**] have found a new way for

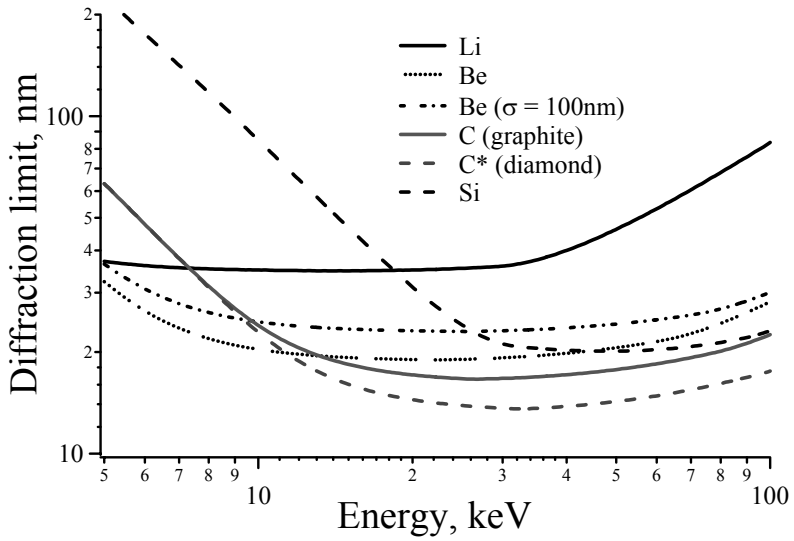

Figure 2.9. Minimal diffraction limits d_t for different lens materials as a function of x-ray energy.

overcoming this limit by gradually (adiabatically) reducing the lens aperture as the size of the beam decreases when it converges to the focus. In this way, the refractive power per unit length increases inside the lens toward its exit approaching a singularity. The resulting numerical aperture can exceed $\sqrt{2\delta}$, allowing one to focus hard x-ray down to 2 nm. The lens design is shown in **Figure 2.10**. A large number of thin lenses is stacked behind each other along the optical axis. To avoid spherical aberration, each individual lens has parabolic shape. As for previous refractive lenses, each individual lens *j* is thin compared to its focal distance

$$f_j = \frac{R_j}{2\delta}. \tag{2.22}$$

Here, R_j is the radius of curvature at the apex of the lens.

For a parabolic lens, other parameters, such as its length l_j, aperture R_{0j}, and minimal

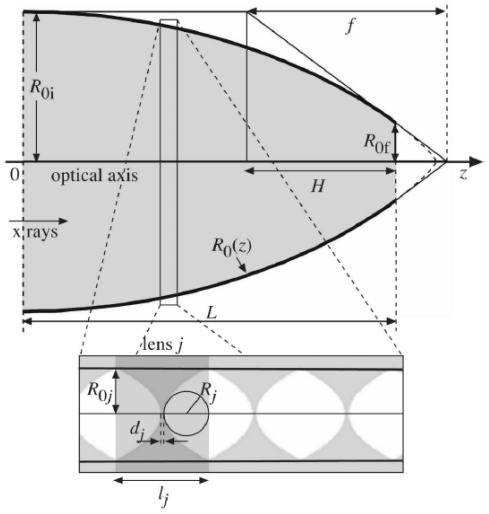

Figure 2.10. Adiabatically focusing x-ray lenses [**Schr2**]. The lens is composed of a large number of individual (parabolic) refractive lenses with gradually decreasing apertures.

thickness d_j, can be related

$$l_j - d_j = \frac{R_{0j}^2}{R_j}. \tag{2.23}$$

To find the aperture R_{0j} as function of position along the optical axis, ray optics can be used. If the number of lenses N is large and the refraction from each lens is small, the path of the ray $r(z)$ inside the lens can be described by the second differential equation

$$r'' = \frac{d^2 r}{dz^2} = -\varpi^2(z) r, \tag{2.24}$$

that is derived from the transfer matrix formalism [**Prot**] in the continuum limit. For the outermost ray, that defines the aperture as a function along the optical axis, the

differential equation (**2.24**) can be written as

$$R_0'' = -\frac{2(1-d_j/l_j)\delta}{R_0}. \tag{2.25}$$

For a parallel beam incident on the first lens, the initial conditions are $R_0(0)=R_{0i}$ and $R_0'=0$, yielding the first order differential equation

$$R_0' = \sqrt{4\delta' \log\frac{R_{0i}}{R_0}}, \tag{2.26}$$

where $\delta' = (1-d_j/l_j)\delta$.

Figure 2.10 shows $R_0(z)$ as a solution of **Equation 2.26**. For a given exit aperture R_{0f}, the lens properties can be calculated, such as the focal distance f, the secondary principal plane H, the effective D_{eff} and the numerical aperture NA in analogy to that of a thin refractive x-ray lens [**Len1**].

$$f = \frac{R_{0i}}{\sqrt{4\delta \log\frac{R_{0i}}{R_{0f}}}},\ H = \frac{R_{0f}-R_{0i}}{\sqrt{4\delta' \log\frac{R_{0i}}{R_{0f}}}}, \tag{2.27}$$

$$D_{eff} = 2R_{0i}\sqrt{\frac{2}{\mu' L}\left(1-\exp\left[-\frac{\mu' L}{2}\right]\right)}, \tag{2.28}$$

where $\mu' = (1-d_j/l_j)\mu$ and μ is the attenuation coefficient.

$$NA = \delta'\sqrt{4\frac{a}{R_{0i}}\left[1-\exp\left(-\frac{R_{0i}}{a}\right)\right]\log\frac{R_{0i}}{R_{0f}}}, \tag{2.29}$$

where $a = \frac{4\sqrt{\delta'}}{\sqrt{\pi}\mu'}$ is a material specific characteristic aperture. The larger a yields the larger numerical aperture, favouring materials with low atomic number Z. The numerical aperture is proportional to $\sqrt{\delta'}$, favouring a lens material with large mass

density ρ. The largest numerical apertures are therefore expected for high density low Z materials, such as diamond or sapphire.

2.2 Main steps and methods in microfabrication process

Lithography for integrated circuit manufacturing is analogous to the lithography in the art world. The slab correspond to masks for the various circuit levels, the press corresponds to the exposure system, the ink may be compared to either the exposing radiation or the radiation-sensitive resist, the paper can represent the wafer into which the pattern will be etched, using the resist as a stencil.

A wide variety of lithographic techniques is used in modern microtechnology to create structures in the micrometer and sub-micrometers range. Here, the basics of microfabrication will be discussed together with some of the techniques.

2.2.1 Typical process outline

Independent of the specific technique, a microfabrication process contains a number of typical steps, which will be outlined here (**Figure 2.11**).

The first step is a choice of the appropriate mask material that protects the areas not to be removed from the attack of the etching medium. Its thickness is determined by selectivity, i.e. by the ratio of the etch rates for the sample and mask material. The mask can be obtained by e-beam evaporation, sputtering or by oxidation of the sample.

Then the sample is coated with a resist that is sensitive to the radiation used in the lithography. A dehydration bake of the sample on a hotplate prior to the coating

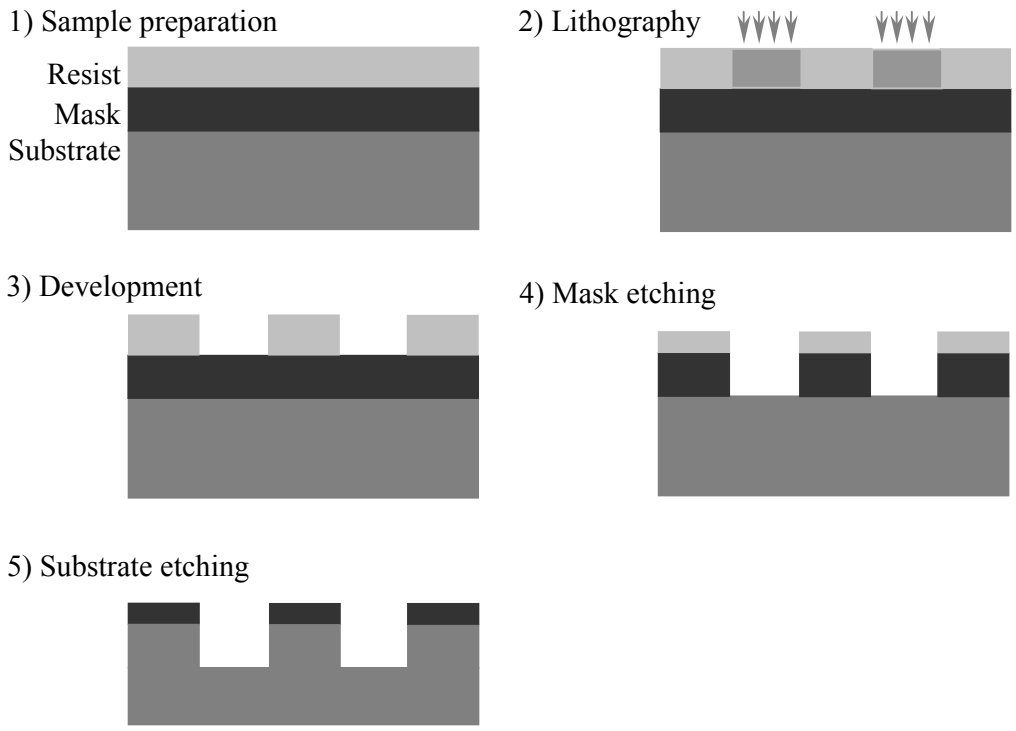

Figure 2.11. Principle steps of a microfabrication process.

enhances the adhesion of the resist on the substrate. After this, the sample is transferred to a spin-coater, where the liquid resist is spread homogeneously onto the surface. The thickness of the layer depends on the viscosity of the liquid and on the rotary frequency of the sample. The resist is finally baked on a hotplate or in an oven to drive out all remaining solvent.

The second step is the exposure of the resist (actual lithographic step). Here, the structure is defined in the resist. This can be done by either moving the beam only over selected parts of the resist (e-beam lithography, **figure 2.12a**) or by a mask shadowing some areas of the resist from the radiation (optical or x-ray lithography, **figure 2.12b**).

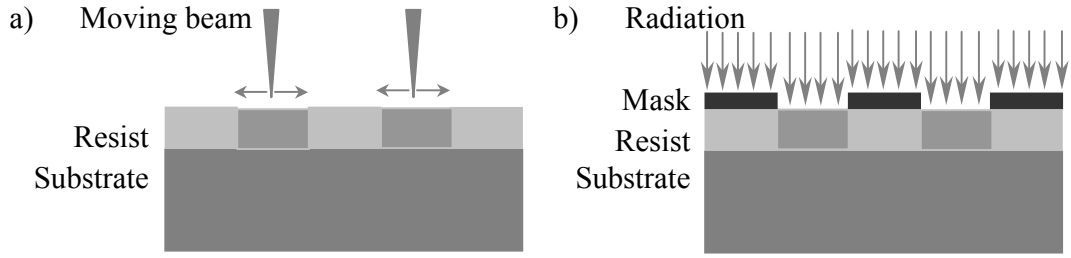

Figure 2.12. a) Lithographic exposure by a moving beam, e.g. of electrons; b) exposure with mask and UV light.

Great care has to be put into the adjustment of the features in respect to the structures already processed on the sample and into the choice of the proper exposure dose. The radiation is able to change the state of the polymers forming the resist and by this to change the solubility of it in some organic solvents [**Clou**]. The reactions appearing in the exposure are mainly chain-scission, cross-linking or the modification of side-groups. Chain-scission, the cutting of polymer chains into shorter pieces, increases the solubility so that a diluted solvent, which would hardly attack the uncut polymers, can wash away the fragments and by this develop a positive structure. Cross-linking on the other hand leads to the building of larger and entangled polymer structures that are more resistant to a solvent and, thus, form a negative mask.

Development in a suitable solvent is the third step in creating the resist patterns. For a positive tone resist, this means that the exposed areas of the resist are washed away (**Figure 2.13a**), while in a negative process the unexposed areas are taken away (**Figure 2.13b**). Especially negative tone resists often require a post-exposure bake prior to the development, which enhances the cross-linking process. A last baking step may sometimes be necessary to enhance the robustness of the resist mask against further processing steps.

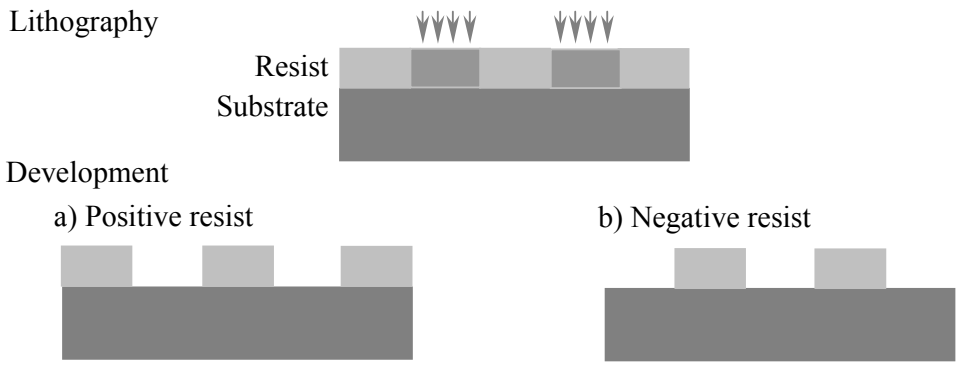

Figure 2.13. a) Development of a positive tone resist; b) development of a negative tone resist.

In the next step, those regions of the mask which are no longer protected by resist are removed to create a pattern in the mask. Removing can be done by wet etching or dry etching [**Köhl**]. The process of the two groups differ in the mobile phase acting as etching medium, i.e. the phase in which the particles from the solid are transferred into and removed from the surface. In wet etching processes the detaching of the material is done by its interaction with a liquid, the "etching bath". Generally wet etchants work isotropically, but there are as well wet chemical etchants with crystallographic preferences that work anisotropically. In dry-etching methods the material is transferred into the gaseous phase. Etching processes working with accelerated ions are subdivided into sputter etching, reactive ion etching (RIE) and various ion beam etching techniques. All etching processes have some criteria in common, that are independent of the material to be etched, the kind of the etching medium and the application. The important parameters are the etching rate and the selectivity, the degree of anisotropy and the degree of sloping of the sidewalls. These parameters shall be introduced in the following.

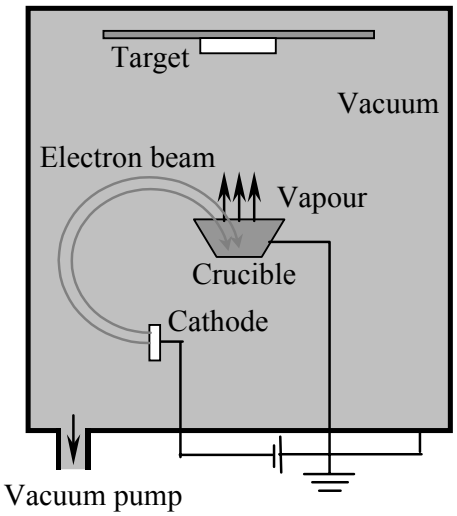

Figure 2.14. Schematic view of an electron beam evaporation system.

Finally, the substrate is patterned by reactive ion etching. Different substrate materials need different gas mixtures for the etching.

2.2.2 Electron beam evaporation

Electron beam evaporation is a common technology for the fabrication of thin metal layers. While small evaporation systems are used in scientific applications, electron beam evaporation is also used on large industrial scale with continuous process flow. For example aluminium, chromium, gold, or titanium are commonly deposited by electron beam evaporation. In the evaporation process a focused electron beam is used to melt and vaporise the desired metal. As shown in **figure 2.14** the electrons are emitted by a cathode and bend on a circular path by a magnetic field. If the metal is continuously evaporated a directed stream of metal vapour from the crucible to the target is formed. When the vapour condenses on the surface of the target a thin film is

created. Thus the three steps of electron beam evaporation process are: evaporation, transportation and condensation. The whole evaporation system has to be maintained under vacuum (10^{-5} to 10^{-9} mbar depending on the deposited material) to prevent contamination of the evaporated layers. Two different evaporation system have been used for this work. One of them was designed and build at II. Physikalisches Institut and is mainly used for the evaporation of chromium, gold, and titanium films. The other one was built at the Forschungszentrum Jülich. This system is suitable for the evaporation of thicker films and was hence used for the deposition of aluminium layers with thickness up to 1 μm.

2.2.3 Electron beam lithography

Electron beam lithography has the possibility of higher resolution than optical lithography because of the small wavelength of the 10-50 keV electrons. The resolution in electron lithography system is not limited by diffraction but rather by electron scattering in the target materials including the resist and by various aberration of the electron optics. Scanning electron beam pattern generators have been under development for more than 30 years and were derived from the scanning electron microscope. Because of the serial nature of the pattern writing, throughput is much lower than for optical systems. However, a wide variety of applications is available in the pattern-generating function for electron beam lithography, such as mask fabrication for optical or x-ray lithography, direct writing on the wafers, and direct reaction with some materials on the substrate. A short outline of the electron beam lithography will be given here. More details can be found in **[Chan]**. The whole setup used for generation, focusing and targeting of the electrons is usually referred to

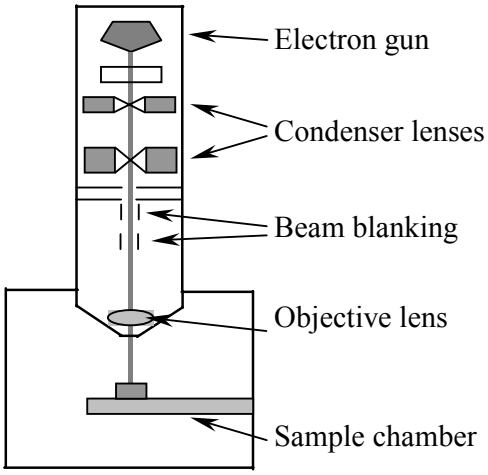

Figure 2.15. Cross-sectional drawing of a typical electron beam column.

as electron beam column. **Figure 2.15** shows a typical design. The electrons are emitted either by heating a filament to the point where the thermal energy of the electrons is sufficient to overcome the work function barrier of the metal or by applying an electric field sufficiently strong that electrons can tunnel through the barrier. The important parameters of the electron gun for electron beam lithography are the virtual source size, the brightness of the source and the energy spread of the emitted electrons. In order to achieve a small spot size, which is necessary for generation of structures in the submicrometer scale the electrons have to be focused. This is achieved by magnetic lenses. The beam is scanned over the surface of the target either by deflection magnets or by electrostatic forces. While magnets introduce less distortions electrostatic deflection can be achieved at much higher speeds. The minimal feature size that can be created with electron beam lithography is mainly limited by electron-solid interactions that occur when the electrons hit the surface of the sample. When electrons collide with the resist they experience many

small angle scattering events, which broaden the initial beam diameter. Electrons even penetrate through the resist into the substrate where large angle scattering (backscattering) takes place. Therefore, the electron dose impinging on a given feature is dependent on the scattering from other features nearby. Larger features receive higher doses than smaller features. This effect is known as proximity effect. As the amount of scattering is dependent on the energy of the impinging electrons the proximity effect is energy dependent. Different methods have been developed, ranging from simply adjusting the overall dose, changing the electron energy to sophisticated dose modulation or mask adjustment techniques. Today, there is a large number of electron beam lithography (EBL) systems available. Modifications range from scanning electron microscopes with integrated EBL to dedicated EBL systems which are mainly used in industry. In this work two different EBL systems were used. One of them is a Philips XL30 scanning electron microscope with an EBL system from Raith Elphy. The other one is a Leica EBPG-5HR designed for high resolution fabrication.

2.2.4 Methods of etching

Wet chemical etching

Wet chemical etching methods for pattering play a key role in microtechniques. They are distinguished from dry etching methods by essentially greater selectivity. This selectivity is due to the specific interactions between components of the liquid and the solid, determining the reaction rate. When dissolving a solid material in a liquid, the components of the solid are transferred into the liquid phase. For this the binding forces between the particles of the solid have to be overcome. The components of the

solid are changed into soluble chemical compounds, which are transported by diffusion and convection off the surface into the interior of the solution. In many cases the solvent molecules themselves form a shell, the solvate shell around the dissolved particles. The solvated particles formed in that way are very mobile by diffusion in the solvent. Three factors, temperature, viscosity, and convection of the liquid, are unspecific parameters influencing all etching rates of a system in the same direction, in contrast to the specifically reacting components of an etchant. By varying the concentration of the rate determining components the etch rate can be adapted in a wide range.

Dry etching – reactive ion etching (RIE)

The particle densities and hence the concentration of reactive chemical components are much lower in the gas phase than in the liquid phase. On the other hand, there are more efficient transport mechanisms in the gas phase. In the RIE-process cations are produced from reactive gases, which are accelerated with high energy to the substrate and which can react chemically with substrate material. Choosing adequate etching gases and excitation conditions, the specific advantages of plasma etching (high selectivity) and of sputter-etching (anisotropic removal) can be combined in the RIE-process. The RIE-plasma can be generated in a planar reactor. The typical construction of the planar plate reactor is shown in **figure 2.16.** The total power is determined by the high frequency-amplitudes, and the removal conditions in the RIE can be influenced by a superimposed direct current-voltage. By this voltage the electrical field can be enhanced in front of the working electrode. In this field the electrons are accelerated to higher energies. The ion energy is limited by collisions in the gas volume. At too high particle densities (higher working pressure) the ions

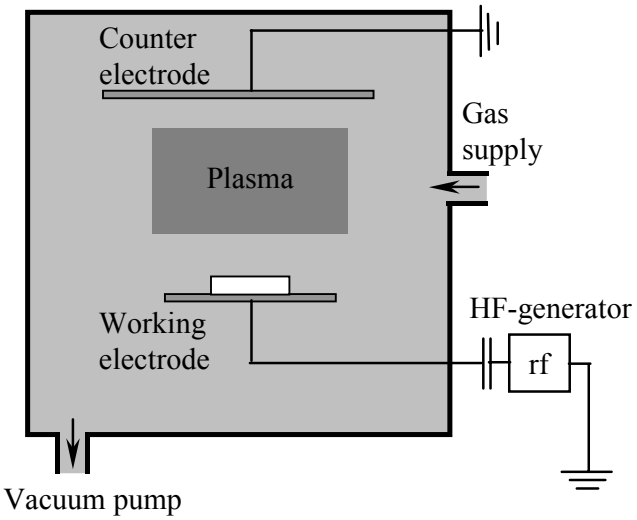

Figure 2.16. Schematic view of a basic RIE system.

loose their energy by repeated collisions and cannot reach the requisite velocities for a good sputter-efficiency. At low pressure the absolute ion density is lower, but it is high in relation to the total number of particles, providing a strongly increased sputter-yield and hence higher etches rates. For a well controlled chemical selectivity, the pressure must not be too low. The contribution of the radicals to the etch removal depends directly on the concentration. The traction of radicals in the total particle number can be enhanced by a high bias. At low pressures, however, the radical concentrations are low at high plasma densities (high relative share of radicals), because the total particle density is low. More details about different mechanisms contributing to the etch removal, to the choice of the etching gas and to the anisotropy can be found in **[Rai]**. In short, to achieve high selectivity, high anisotropy, high mask stabilities, and high etch rates for etching metal films, there is a tendency to apply low pressures and high plasma densities. The necessary etch reactors work with pressures in the range of 0.13 to 2.6 Pa, at 0.5 Pa, preferably.

Chapter 3

Optimised fabrication of silicon parabolic nanofocusing x-ray lenses (NFLs)

In the last years several papers have been published addressing the question of an ultimate limit of the focal size which can be achieved in x-ray optics [**Schr2**], [**Ber**]. Up to now, the theoretical limit has not yet be reached experimentally. For refractive lenses in the form of parabolic cylinders, etching of trenches often results in not perfectly vertical sidewalls and this implies a blurred focus. For Fresnel zone plates, the resolution is given by the width of the smallest outer zone, values under 60 nm are difficult to achieve. This chapter describes a significantly improved deep reactive ion etching process for the fabrication of nanofocusing parabolic refractive lenses made of silicon.

3.1 Design of silicon NFLs

For the purpose of imaging with hard x-rays in the energy range from 10 to 100 keV parabolic refractive beryllium and aluminium lenses are excellently suited because

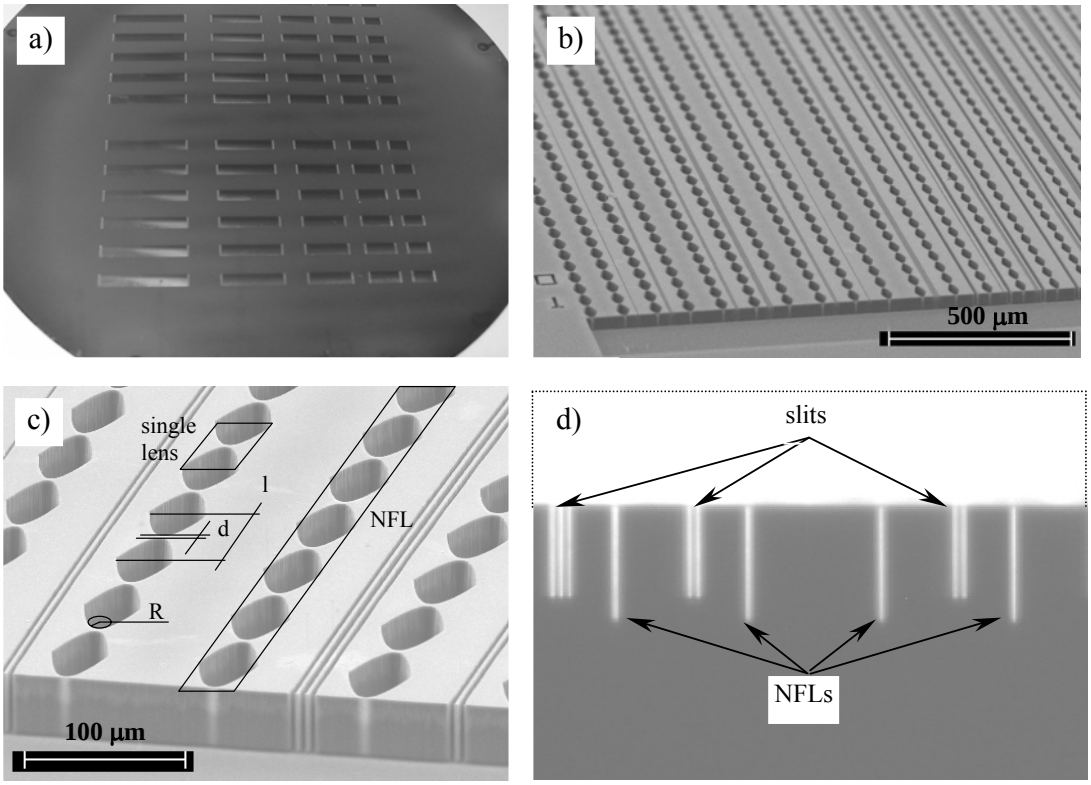

Figure 3.1. Nanofocusing refractive x-ray lenses made of silicon: a) 4 inch silicon wafer with 60 lens blocks. Horizontally, the number N of single lenses in one NFL is varied. Starting from the right, the blocks contain NFLs with 35, 50, 71, 100, and 142 single lenses each. From the bottom to the top, different mask corrections from 0 to 500 nm in steps of 100 nm are applied; b) SEM micrograph of one block. Each block has 21 NFLs with different radii of curvature from 1.0 µm to 5.0 µm in steps of 0.2 µm; c) SEM micrograph of a part of a block. Different numbers of trenches between two lenses are used to identify a lens with a given curvature; d) Using a high resolution x-ray camera one is able to easily find and align a given lens.

they have rotational symmetry about the optical axis [**Len2**]. This results in images free of spherical aberration and other distortions. However, for the generation of a very small focal spot, nanofocusing refractive lenses (NFLs) with crossed parabolic cylinder symmetry are more appropriate [**Schr1**]. They are made of a number single parabolic cylinder lenses etched behind each other into the lens material (**Figure 3.1**). The most outstanding feature of these lenses is their small radius of curvature R, (**Figure 3.1c**) that lies in the micrometer range and leads to focal distances in the centimetre range for hard x-rays [**Schr1**]. In order to provide flexibility concerning the choice of the focal length and of the photon energy, different numbers of single lenses in one nanofocusing lens (NFL) and different radii of curvatures are required. **Figure 3.1** shows typical NFLs made of silicon. The number of single lenses in different NFLs was 35, 50, 71, 100, 142 (**Figure 3.1a**). The radius of curvature R varies between NFLs in a block from 1 μm to 5 μm with steps of 0.2 μm, resulting in 21 different NFLs per block (**Figure 3.1 b**). The thickness d of a single lens on the optical axis (cf. Fig. 1c) is about 5 μm and its overall length l is 85 μm. Different numbers of trenches between two NFLs are used to identify a lens with a given curvature (**Figures 3.1c** and **3.1d**.). Due to a proximity effect by e-beam lithography and underetching of the mask in the deep reactive ion etching step the lithographic process leads to slight deviations between the electronic mask for electron beam lithography and the resulting final shape of the lenses. This deviation was modeled as a homogeneous shift (**Figure 3.2**). As the size of this shift was not apriori known, six sets of lens blocks with different corrections were written (**Figure 3.1a**). The mask corrections were varied from 0 to 500 nm in steps of 100 nm.

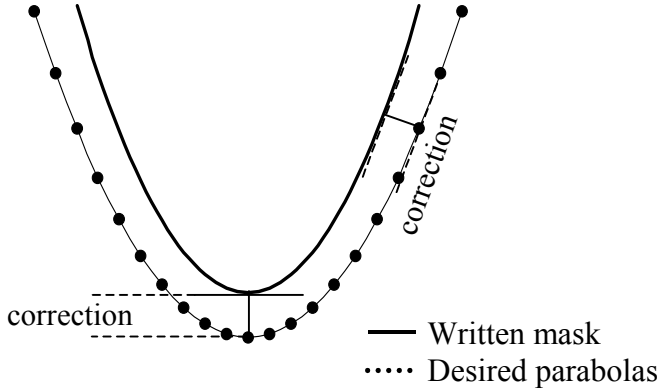

Figure 3.2. Schematic representation of the correction of a written mask for e-beam lithography. For exposure each point on the parabola was transferred to the inside by an amount equal to the correction. Corrections were 0, 100, 200, 300, 400 and 500 nm.

3.2 Fabrication of silicon NFLs

The main fabrication process for NFLs made of silicon is deep trench reactive ion etching. The process used here is a switched process, known as Bosch process, time multiplexed deep etching [**Ayón**] or gas chopping etching technique [**Vol**]. In general, it consists of a cyclic repetition of a passivation phase, which protects sidewalls from being etched, and an etch phase which is isotropic. Cryogenic etching [**Boer**] could be an alternative, but was not available. Nowadays, the multiplex process is successfully used in MEMS industry, however its application for the fabrication of x-ray optics needs careful selection of process parameters which are described below.

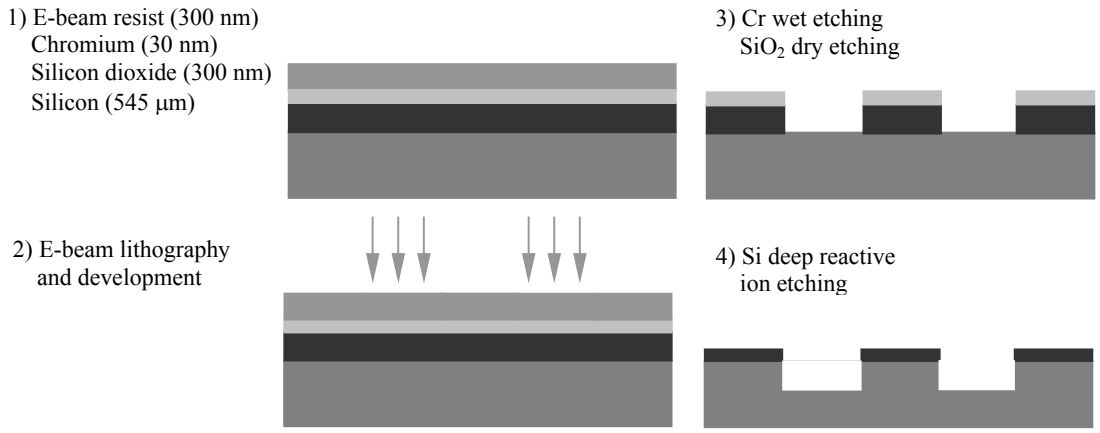

Figure 3.3. Fabrication process of silicon refractive lenses.

In contrast to the first nanofocusing x-ray lenses made of silicon [**Schr1**], the present microfabrication process started with 4 inch silicon wafers which are wet oxidized at the temperature of 1050 °C to obtain a 300 nm silicon dioxide layer on the surface. This layer serves as a mask for the etching of the lens structures into the silicon. As a mask for the SiO_2 we have evaporated a 30 nm thick chromium layer on top of the SiO_2 using electron beam evaporation (**Figure 3.3**, step 1). Subsequently, the wafer was spin coated with a positive e-beam resist PMMA 600K deposited by means of a Semitec CPS20 spin-coating system. The coating was done during 30 s spinning the wafer at 6000 revolutions per minute. Then the resist was baked on a hot plate at 125 °C for five minutes and cooled down. The process was repeated in order to obtain a double coated wafer. The coated wafer was structured by electron beam lithography (EBL) on a LEICA machine EBPG5HR at 50 kV exposure energy. To obtain a high writing speed the inner region of the lens was written with a beam size of 350 nm and an exposure dose of 200 $\mu C/cm^2$ whereas the edges (width 2.5 μm measured from the

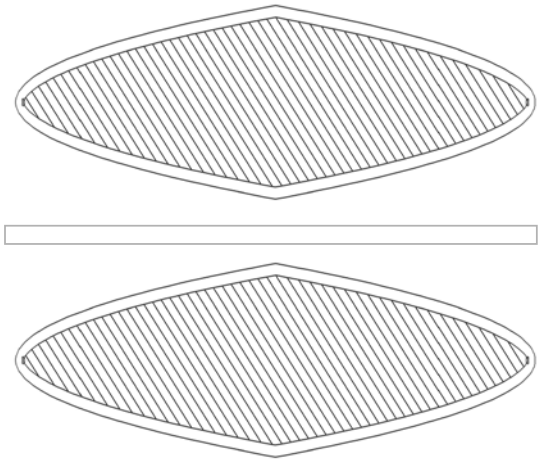

Figure 3.4. Schematic representation of the Si-lenses made by e-beam lithography. The filled regions were written with a beam size of 350 nm and a dose of 200 $\mu C/cm^2$. The edges were written with a beam size of 40 nm and a dose of 310 $\mu C/cm^2$.

edge of the mask) were written with a beam size of 40 nm and an exposure dose of 310 $\mu C/cm^2$. The lateral resolution of the beams was 250 and 25 nm for the inner and edge regions, respectively (**Figure 3.4**). After e-beam writing the sample was developed in the fast developer AR 600-55 for 45 s (**Figure 3.3**, step 2)

The chromium layer of 30 nm was structured in a mixture of ammonium cerium IV-nitrate and of perchloric acid (chromium-etch 3144) at room temperature for 25 s corresponding to an etch rate of about 75 nm/min (**Figure 3.3**, step 3) . The end point was detected visually by a change of colour on the surfaces (from metallic for chromium to lilac for silicon dioxide). To stop the etching process the sample was transferred to distilled water at room temperature. Then the resist layer was removed in an acetone bath. The underlying SiO_2 was etched (**Figure 3.3**, step 3) in a Plasmalab

System 100 ICP180 etch tool from Oxford Instruments. In this step, a pressure of 0.43 Pa, ICP power of 1300 W and rf bias of 50 W were used. The process gas mixture contained 15 sccm trifluormethane (CHF_3) and 18 sccm tetraflourmethane (CF_4). The etch time was 6 min.

Next, the silicon etch requires careful selection of process parameters in order to achieve vertical sidewalls with minimum sidewall roughness, minimum underetch and high etch depths. Various attempts for obtaining smooth vertical sidewalls are known: additional flow of argon during the etch phase, reduced cycle time, variation in switching between passivation and etching (overlap) [**Liu**], etch depth dependent changing parameters (multi step process, parameter ramping) [**Chab]**, [**Hop**]. To obtain a large trench depth a high selectivity is essential. Known possibilities to increase the mask selectivity are higher etch pressure (promoting micrograss), reduced ion energy, reduced substrate temperature (affecting passivation film quality) or shifting the etch balance towards passivation (leading to vertical striations on the sidewalls). Another possibility is the use of an aperture inside the reaction chamber which mainly alters the ion flux thereby enabling higher etch selectivity. Prediction of etch results in dependence of the process parameters is difficult as substrate properties change, such as the amount of silicon area to be etched or the trench width.

Due to a limited number of samples the starting point within parameter space should be a robust recipe and, at the same time, as close as possible to the optimum to be achieved. Therefore, a proven recipe with relatively short cycle time and good selectivity was chosen. Deep silicon etches (**Figure 3.3**, step 4) were performed at a Multiplex ICP standard rate etch tool from Surface Technology Instruments equipped with an aperture of 120 mm diameter. Conditioning runs were performed before the main etches. Process parameters used were 6 s etch phase duration, 130 sccm

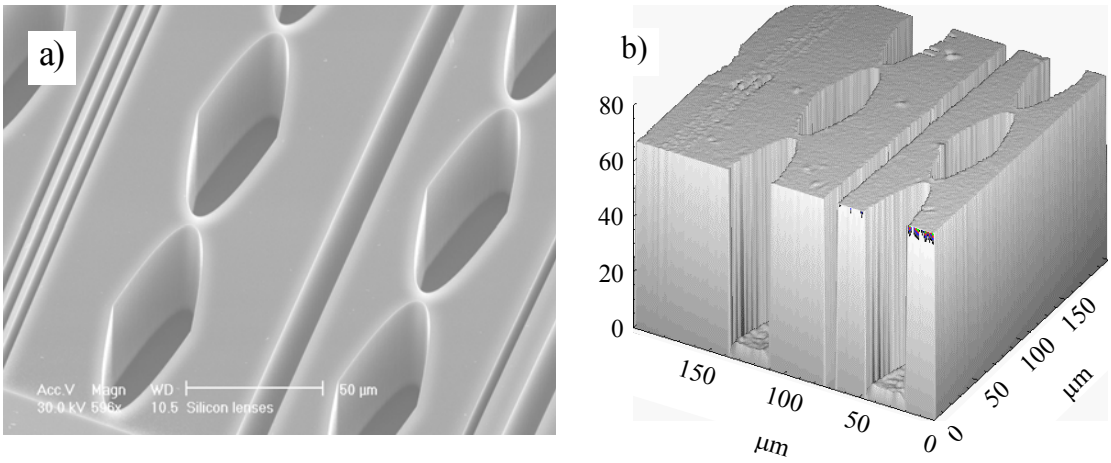

Figure 3.5. Determination of the lens depth: a) Due to the small area and large depth of the lenses depth determination by electron micrograph is not possible without breaking the lenses; b) However, the lens depth was successfully determined by FRT and turned out to be 62 µm.

SF_6, 2.4 Pa, 600 W ICP, 12 W platen power and 5 s deposition phase duration, 120 sccm *c*-C_4F_8, 1.9 Pa, 600 W ICP, no platen power. As a result of 30 min etching, a lens depth of 62 µm (**Figure 3.5**), a mask consumption of less than 200 nm, and a side wall roughness of less than 150 nm were achieved.

3.3 Analysis of the radius of curvature of the lenses

There are two critical points in manufacturing NFLs. The first one is the form fidelity of the parabolas and the second in the steepness of the sidewalls. Compared to our first silicon NFLs [**Schr1**] both parameters have been improved substantially in the present work (**Figure 3.6**). By using a modern writing system (LEICA machine

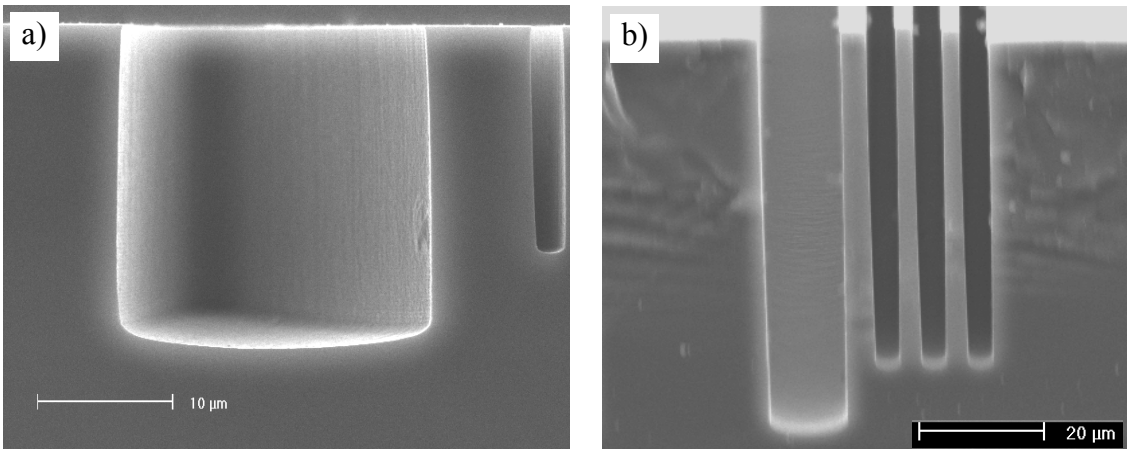

Figure 3.6 a) First nanofocusing lenses made of silicon. Due to a small wafer size (2 cm × 2 cm) and the resulting non-optimal contact between the wafer and the plate in the reactive ion etching chamber, the depth was only 23 µm. The lens surfaces are also slightly curved. b) Nanofocusing lenses made on a 4 inch silicon wafer. Due to better contact between the sample and the plate in the reactive ion etching chamber the depth was increased to 62 µm. In addition vertical flats are obtained.

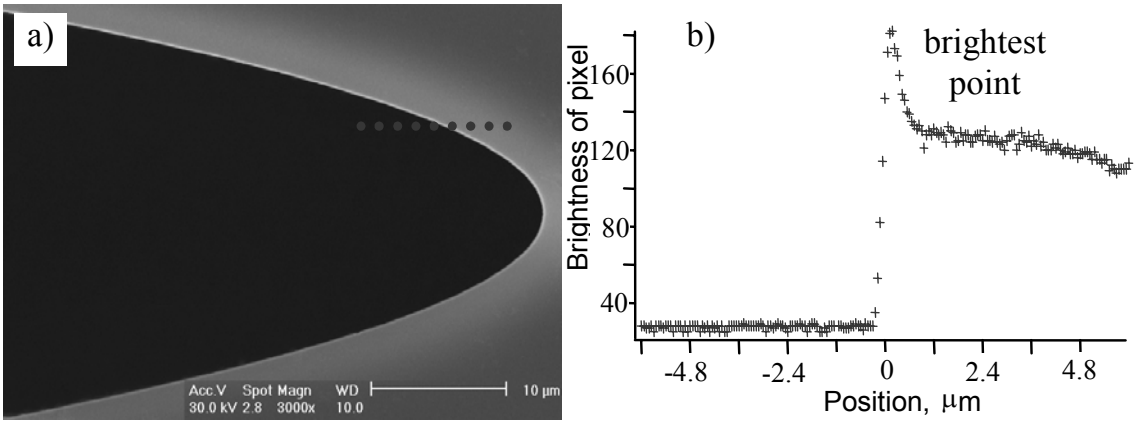

Figure 3.7. a) SEM micrograph of half of a single lens (R=3.0 µm). b) The brightest point on the curve corresponds to the edge of the lens.

EBPG5HR) the 4 inch wafer processing has become possible. A replacement of small samples (sample size of 2 cm x 2 cm) by 10 cm wafers led to an increased etching depth (from 23 μm to 62 μm) and an improved steepness of the sidewalls.

In order to determine any deviation between the electronic mask for e-beam lithography and the resulting final shape of the lenses as well as to quantify the quality of the new NFLs we have made SEM micrographs. From these micrographs, the lens shape was extracted by a series of line scans across the edge of the lens, as indicated in **figure 3.7**. The intensity of the reflected electrons increases drastically when going from the bottom to the top of a trench. We observe a distinct intensity peak at the edge itself (**Figure 3.7b**). The position of this peak was identified with the position of the edge. The shape of a parabola in the vicinity of the apex is shown in **fig. 3.8a**, together with a parabola fitted to the data. In this way, from the e-beam lithography data the radius of curvature R of 3.0 μm was expected. The lenses with the corresponding value of radius of curvature were identified. The deviation between the electronic mask for e-beam lithography and the resulting final shape of the lenses is close to 270 nm.

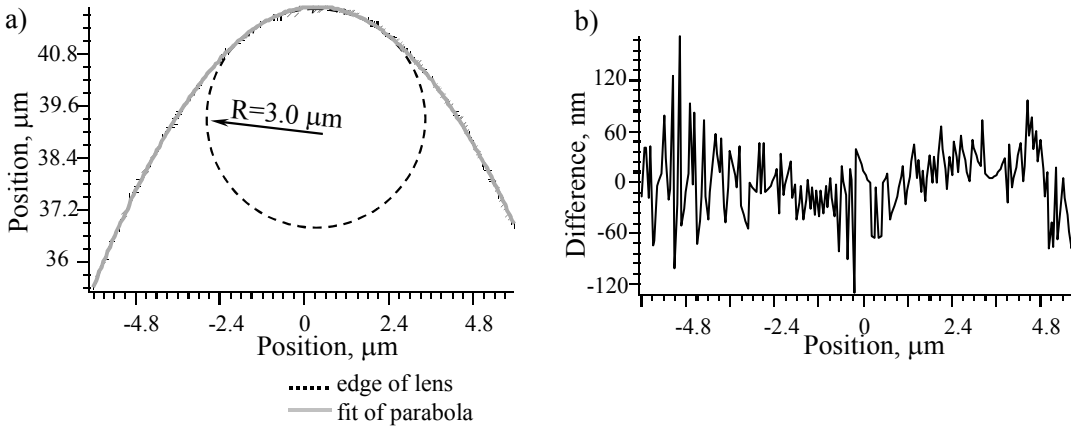

Figure 3.8. a) Fit of the lens shape to a parabolic function. b) The difference between the lens shape and parabolic function shows minimal discrepancy.

3.4 Lens setup

A typical setup for nanofocusing refractive x-ray lenses is shown in **figure 3.9**. The lenses are placed at a distance L_1 (40-50 m) from the source. Both lenses (horizontal and vertical) have six degrees of freedom (3 translations and 3 rotations). During the experiment the alignment of NFLs can be done using a high-resolution x-ray CCD camera. A Pt pinhole (thickness of 250 μm, diameter 23 μm) has two translation degrees of freedom for an adjustment and must be positioned around optical axis behind the lens setup.

The horizontally or vertically focusing lens produces its focus at a focal distance f_h and f_v from the centre of the lens, correspondingly. To focus in the same plane (perpendicular to the optical axis), both NFLs must have different focal length. This

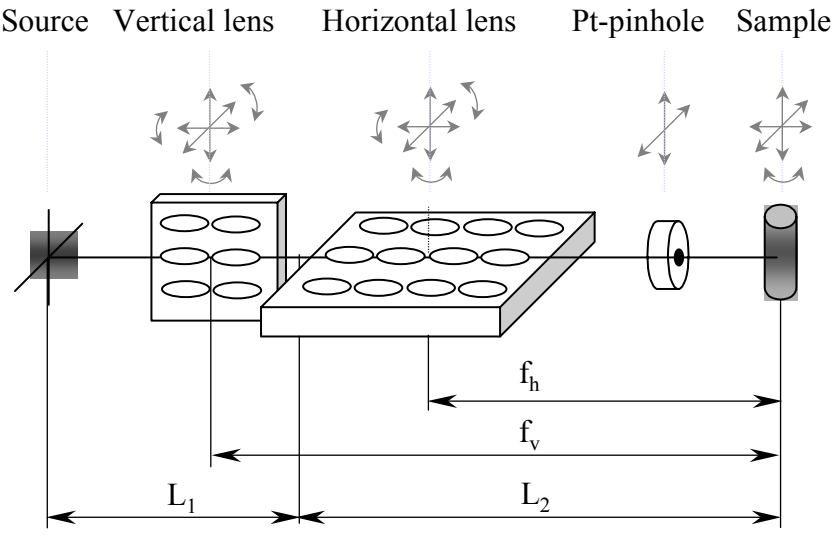

Figure 3.9. Schematic sketch of an experimental arrangement with nanofocusing lenses. Two lenses perpendicular to each other must be aligned to focus in one plane.

is achieved by NFLs with a different number of lenses, e.g N=70 for the vertically and N=100 for the horizontally focusing lenses. Then the fine alignment is done by the different radii of curvature R for the lens arrays. The specific values to be chosen depend on the x-ray energy and other experimental details.

The sample is placed at a distance L_1+L_2 from the source. At the same time, this distance L_1+L_2 serves as focal plane for both lenses. The sample stage needs three translational degrees of freedom for the experiments with nanofocusing or nanodiffraction and an extra rotational degree of freedom for experiments with fluorescence tomography.

3.5 Focusing properties of Si NFLs

The silicon nanofocusing lenses were tested at the low-β beamline ID13 of the European Synchrotron Radiation Facility (ESRF). The synchrotron source size was ≈ 150 μm x 60 μm full width at half maximum (FWHM) and the distance between the source and the lens setup was 47 m. Two different energies were used. In the first case, at 21 keV, an NFL with N=100, a total length of 8.4 mm and a radius of curvature R=2.0 μm was used to focus the beam horizontally. The image distance L_{2h} from the centre of the NFL to the focal spot was 10.7 mm. For the vertical focusing a NFL with N=71 was used what corresponds to a lens length of 6.0 mm. The radius of curvature R for the vertical direction was determined to be 2.86 μm. This yields an image distance L_{2v} of 19.4 mm.

The vertically focusing NFL was placed in front of the horizontally focusing one to get the same focal plane for both lenses (**Figure 3.10**). In the focus, at 200 mA ring current, a flux $\Phi_f=1.7\cdot10^8$ ph/s and a lateral size of 47 nm by 55 nm were measured as

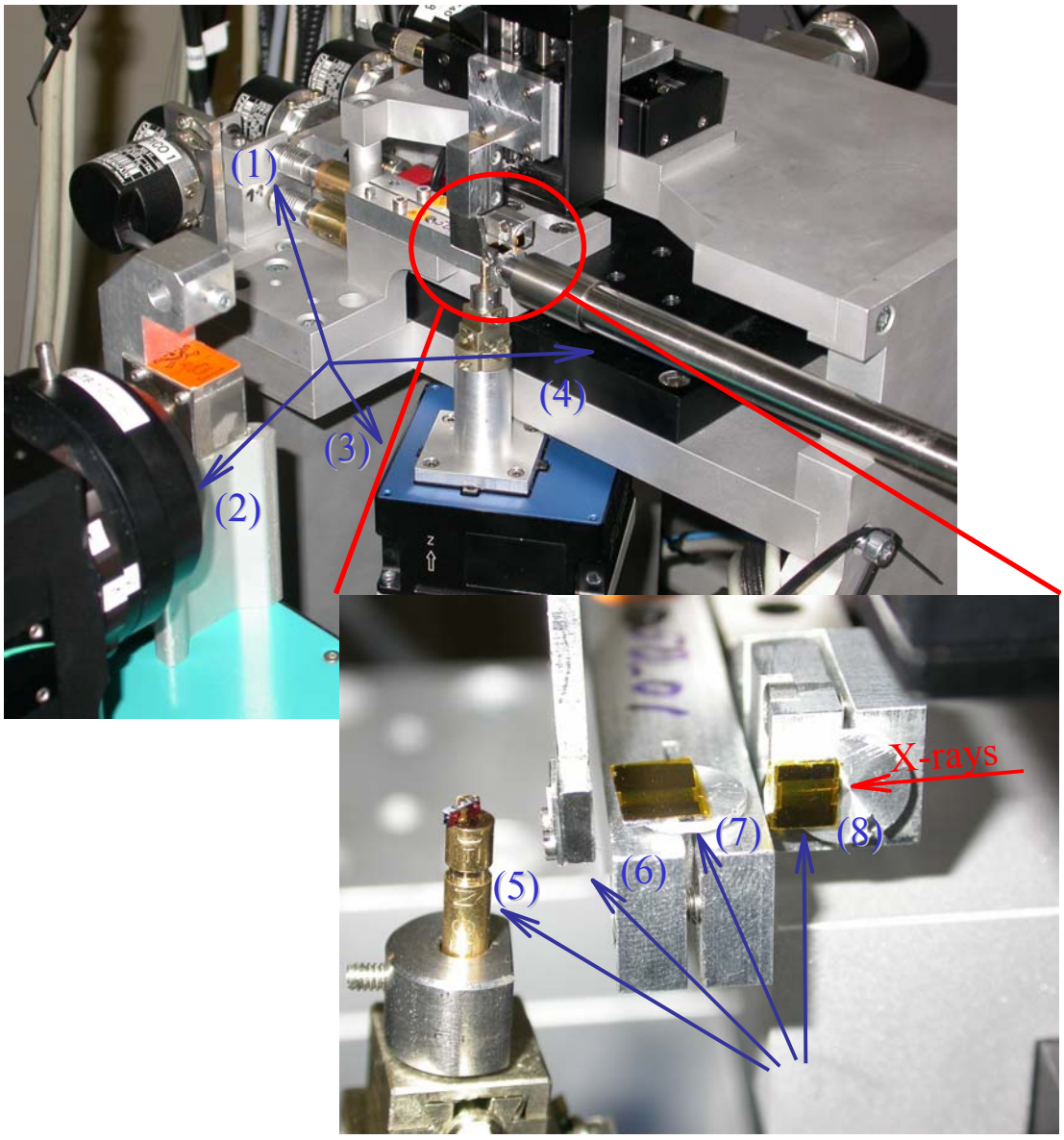

Figure 3.10. Experimental setup with silicon nanofocusing lenses as implemented at ESRF/ID13. (1) Picomotor stage with encoders for the alignment of the vertical lens, (2) high resolution camera, (3) nanocube, (4) fluorescence detector, (5) sample holder, (6) aperture, (7) horizontal lens, and (8) vertical lens.

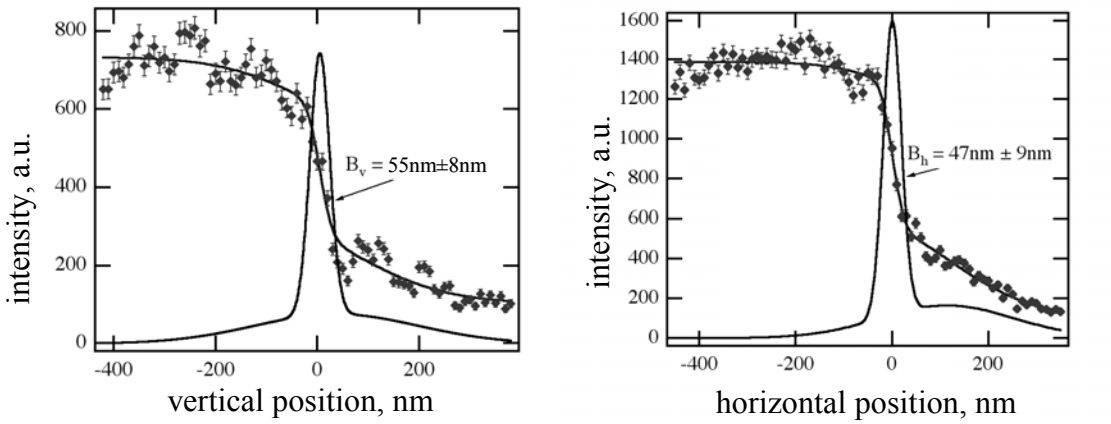

Figure 3.11. (a) Horizontal and (b) vertical beam profile determined by fluorescence knife-edge scans.

compared to

an expected size of 43 nm by 51 nm. **Figure 3.11** shows the vertical and horizontal scans of a gold edge through the microbeam. As the gold knife-edge is scanned through the beam, its gold fluorescence radiation is detected by an energy sensitive detector facing the knife-edge perpendicular to the beam.

The second experiment was done at 15.2 keV. To focus the beam horizontally 50 single lenses were used in one array with radius of curvature R=2 μm and total lens length of 4.2 mm. The image distance L_{2h} from the centre of the NFL to the focal spot was 10.27 mm. A NFL with N=35 for the vertical focusing was used that has a length of 3.0 mm. The radius of curvature R for the vertical direction was determined to be 3.2 μm. This yield an image distance L_{2v} of 22.28 mm. In the focus, a flux Φ_f=1.3·10^8 ph/s and a lateral size of 183 nm by 107 nm were measured (expected of 60 nm by 80 nm). The discrepancy between the expected and obtained focal is

probably due to setup instabilities. **Table 3.1** gives details for both experiments. The setup was used to perform nanodiffraction of phase change media (see **Section 4.1**) and micromirrors (see **Section 4.2**).

Table 3.1. Experimental details for the lenses test.

X-ray source				
Energy, eV	21000		15200	
Source size, h × v, μm × μm, FWHM	150 × 60			
Distance between source and lens setup, m	47			
Flux, ph/s/mm^2	10^{12}			
Nanofocusing lens	horizontal	vertical	horizontal	vertical
Number of single lens (N)	100	71	50	35
Radius of curvature (R), μm	2.0	2.86	2.0	3.2
Distance between two single lenses (d), μm	4			
Length of single lens (w), μm	85			
Lens properties				
Focal distance, mm	10.7	19.4	10.3	22.3
Focus size, nm	43	51	59	80
Measured focus size, nm	**47**	**55**	**183**	**107**
Geometrical demagnification	**4400**	**2400**	**4580**	**2100**
Flux in focus, ph/s	**1.7×10^8**		**1.3×10^8**	

Chapter 4

Application of silicon nanofocusing x-ray lenses

The main applications of silicon nanofocusing x-ray lenses lie in scanning microscopy and microanalysis with hard x-rays [**Schr4**]. They allow one to perform x-ray analytical techniques, such as diffraction, fluorescence analysis, and absorption spectroscopy with high spatial resolution [**Schr5**]. While nanofocusing lenses are ideal for microbeam applications, they are not well suited for high quality full field imaging because of distortions in the image due to the crossing of two cylinder lenses with different focal lengths [**Len4**].

4.1 Nanodiffraction from laser modified films

$Ge_2Sb_2Te_5$ is one of the materials currently used for phase change recording [**Ich**]. In these materials a reversible phase change is used for rewritable optical data storage. To write a bit, the crystalline material is locally molten by a laser beam of appropriate intensity. Subsequent quenching into the amorphous phase can be achieved by avoiding recrystallization due to rapid cooling. To erase a bit, the amorphous area has

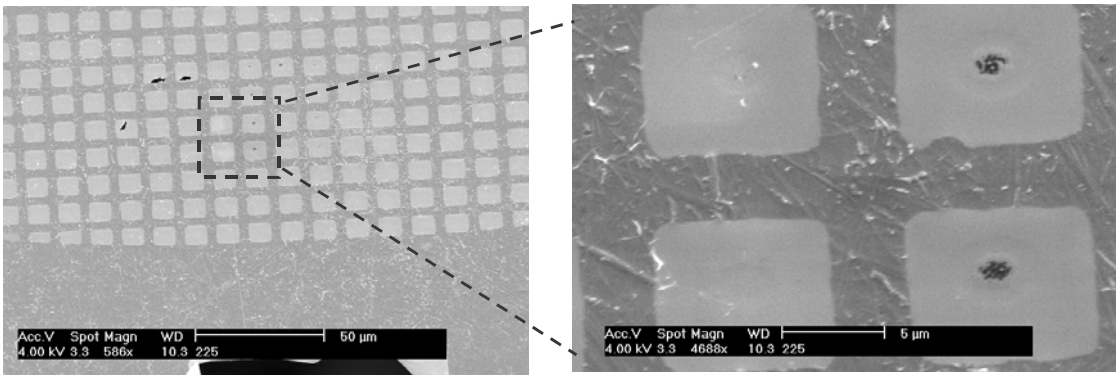

Figure 4.1. Scanning micrograph of an amorphous $Ge_2Sb_2Te_5$ matrix with laser modified areas. The thickness of the film is 80 nm. A 2000 Cu-mesh was used to identify the given bit more easily.

to be heated for a sufficiently long time above the glass transition temperature by a laser beam of a lower intensity, so that recrystallization can take place. The two phases can be distinguished by their different reflectivity in the visible light range.

Presently the most favoured materials are Te-based alloys like the ternary alloys of the quasibinary line of $GeTe$-Sb_2Te_3 ($Ge_2Sb_2Te_5$ or $GeSb_4Te_7$) [**Yama**] or AgInSbTe [**Shin**]. These materials have to fulfil a number of requirements to achieve faster recrystallization.

In this work, x-rays from a third generation synchrotron radiation source were focused by silicon nanofocusing x-ray lenses. X-ray diffraction from a very small volume (about of 10^7 atoms) allowed to determine the lattice parameter changes during laser induced crystallization in the amorphous films. This is of particular interest for $Ge_2Sb_2Te_5$ as it was shown by temperature dependent electrical measurements that this material undergoes a structural transformation at 310 C from a

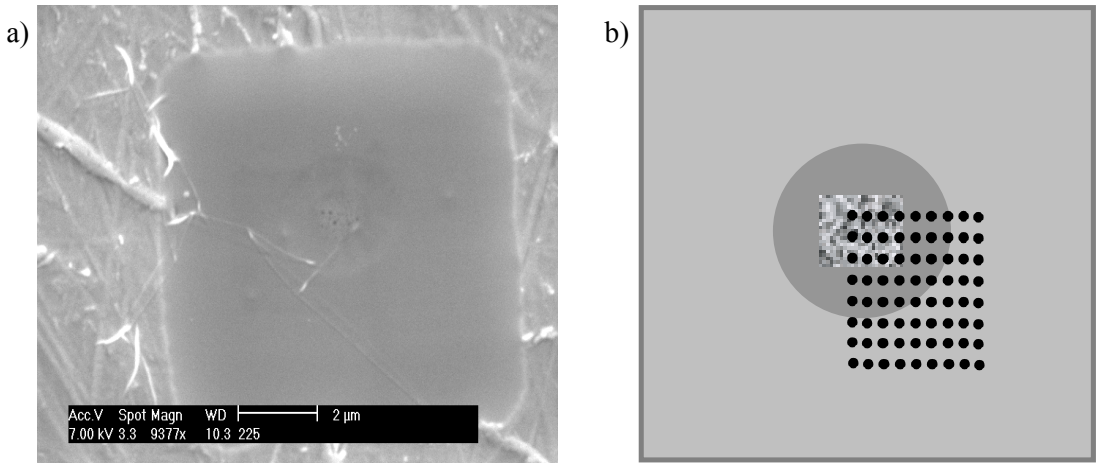

Figure 4.2. a) Scanning electron micrograph of laser induced polycrystalline microstructure ($Ge_2Sb_2Te_5$) in an amorphous film. b) Schematic sketch of a mesh – scan (9 × 9 points, step of 0.5 µm, exposure time per point of 90 s) through the laser induced polycrystalline microstructure ($Ge_2Sb_2Te_5$) in amorphous film.

cubic to a more complex hexagonal structure [**Fri1**]. It was the purpose of the study to identify the crystalline phase in the laser modified areas, as both crystalline phases have slightly different optical properties. Furthermore, the small focal spot (of about 100 × 100 nm^2) allows to study the lattice parameter in different locations of the laser irradiated bit size (about of 3 µm in diameter). The thickness of the analysed AgInSbTe and $Ge_2Sb_2Te_5$ films was about 80nm (**Figure 4.2a)**.

4.1.1 Experimental procedure

The experiment was carried out by means of silicon nanofocusing parabolic refractive x-ray lenses at ID13 (ESRF). An NFL setup, similar to that of section 3.5, was used at

15.2 keV photon energy in the present investigation. The irradiated volume had a size of 100 nm x 180 nm x 80 nm (0.0016 μm^3) what corresponds to about 10^7 atoms. To investigate the crystallization - induced changes in the interplanar spacing of the films, two modifications of the samples were used: a polycrystalline film and a laser induced crystalline microstructure in an amorphous film. To compare the interplanar spacing of $Ge_2Sb_2Te_5$ in the centre and along the edges of a laser induced polycrystalline microstructure, a mesh-scan (9 x 9 points, step of 0.5 μm, exposure time of 90 s per point) was carried out (**Figure 4.2b**). The diffraction patterns were analysed with the program FIT2D [**FIT2D**], which was calibrated with a silicon standard sample. The calibration of FIT2D was verified by diffraction from a polycrystalline copper sample. Note that there are several reflexes in the centre of the

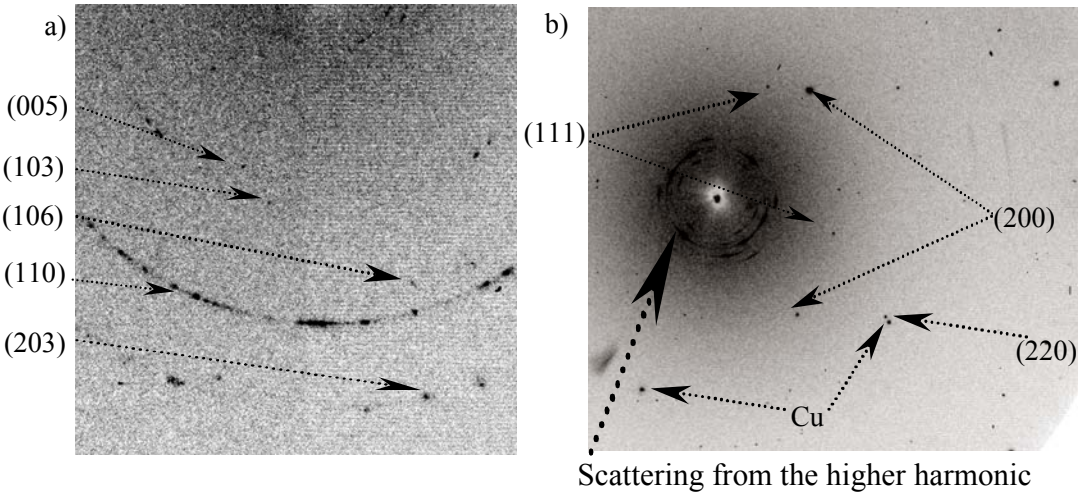

Figure 4.3. a) Diffraction from the polycrystalline AgInSbTe reference sample (exposure time of 60s). b) Diffraction from a laser induced polycrystalline microstructure ($Ge_2Sb_2Te_5$) in amorphous film (exposure time of 90 s).

diffraction pattern (**Fig. 4.3b**). They are due to higher harmonic in the beam and are neglected in the sample analysis.

4.1.2 Results

Diffraction from the polycrystalline AgInSbTe reference sample (a hexagonal structure, similar to that of Sb_2Te, exposure time of 60 s) is shown in **Figure 4.3a**. Corresponding interplanar spacings d are given in the **Table 4.1**. The experimental and theoretical d values show reasonable agreement.

Table 4.1. Interplanar spacing for analysed samples.

AgInSbTe			$Ge_2Sb_2Te_5$		
(*hkl*)	d (Å)*	d (Å)	(*hkl*)	d (Å)*	d (Å)
005	3.44	3.43	111	3.47	3.46
103	3.10	3.06	200	3.00	3.00
106	2.25	2.24	220	2.12	2.10
110	2.14	2.10	311	1.81	1.82

*-expected value for bulk samples

The typical diffraction pattern for the laser induced crystallization samples ($Ge_2Sb_2Te_5$, exposure time of 90 s) is shown in **Figure 4.3b.** The corresponding d values are listed in **Table 4.1**. Measurement of the diffracted intensities shows that the crystal structure has cubic symmetry and that the corresponding interplanar spacing are close to the theoretical ones. Moreover, only several reflections (**Figure 4.4**)

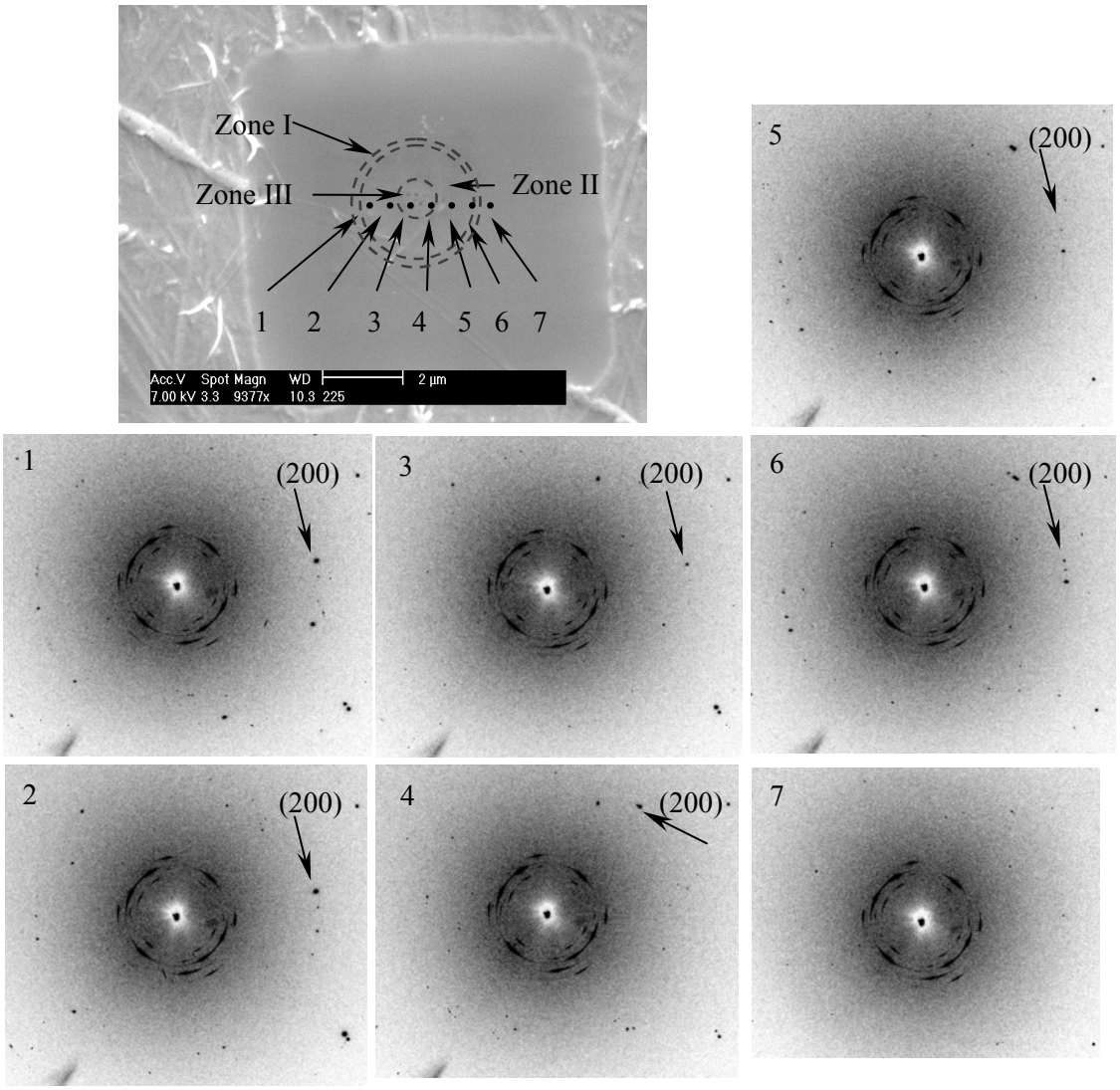

Figure 4.4. Schematic sketch of morphology of the crystallized area and diffraction patterns for the laser induced crystallization samples ($Ge_2Sb_2Te_5$, exposure time of 90 s) by varying of the spot position through the bit (points 1-7).

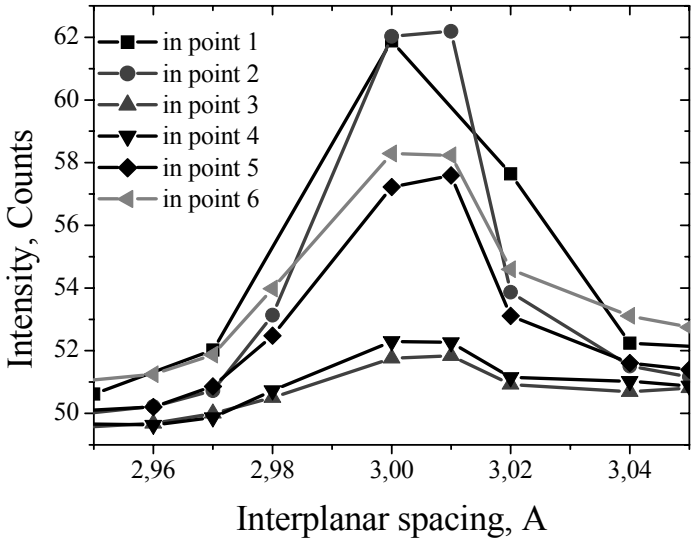

Figure 4.5. Diffracted intensity of the (200) reflection by the different spot position for the laser induced crystallization samples ($Ge_2Sb_2Te_5$, exposure time of 90 s).

rather than rings are observed in the diffraction pattern. This implies that only a few grains in the crystallized area were irradiated that fulfil the Bragg condition. Their sizes are similar to the size of the focal spot (about of 100 nm). Varying the spot position from point 1 to point 6 in steps of 500 nm (**Figure 4.4**) generates different reflections in the diffraction patterns, without changes in the lattice parameters. This means that a different grain in the bit was hit by the beam. The point 7 is positioned outside of the laser induced bit, i.e., in the amorphous film resulting in no diffraction peaks (**Figure 4.4,** 7). We have observed a variation in peak intensity with the location of the grains in the crystallized area, as illuminated for the peak (200) in the **figure 4.4** and **figure 4.5**. A decreasing intensity corresponds to a downsizing of the

irradiated polycrystals and the smallest polycrystalline size is observed in the points 3 and 4.

4.1.4 Discussion

The results (**Figure 4.5**) agree with the morphology of the crystallized area where three different zones can be distinguished [**Fri2**]. Zone I consists of small crystalline grains located at the border of the surrounding amorphous matrix. This zone could be not defined in our experiment due to the minute amount of these grains and their small size (about of 5-25 nm). Zone II is characterized by elongated radially arranged crystalline grains (between 0.1 and 1 μm), and Zone III with grain sizes below 0.1 μm was qualitatively identified (**Figure 4.4**, top).

4.1.5 Conclusion

The applied technique makes possible an analysis of the structural transformations in thin films of the phase change media. The illuminated volume was reduced to 180 nm × 100 nm × 80 nm, which corresponds to ~10^7 atoms. In general, more diffraction patterns should be made for a reliable analysis of the experimental data. In future, nanofocusing x-ray lenses allow for the investigation of the time dependence of the crystallization process and for the influence of the temperature – time variation in the laser modified areas.

4.2 X-ray stress analysis for a free standing Al-mirror

Different microsystems have been developed which only have in common that they are fabricated by process known from semiconductor technology. There is a trend of designing ever smaller sized systems. The knowledge of material properties that has been gathered in mechanical engineering cannot be used for microsystems because often thin structured layers are involved. Their properties are rather different from those of bulk material and even of lateral extended thin films.

The residual stresses and their distribution across the micro-mirror blade (**Figure 4.6**) will play a central role in understanding the structural relaxation in Al-mirrors of less than a half micron thickness. The averaged residual stresses in an array of free standing mirror blades were determined by the laboratory x-ray facility [**Sch**]. To investigate residual stresses at individual mirrors, the stress state in 2 μm broad hinges holding the mirror blades is especially of special interest. A stress analysis by micro-focus x-ray diffraction is required [**Tam**].

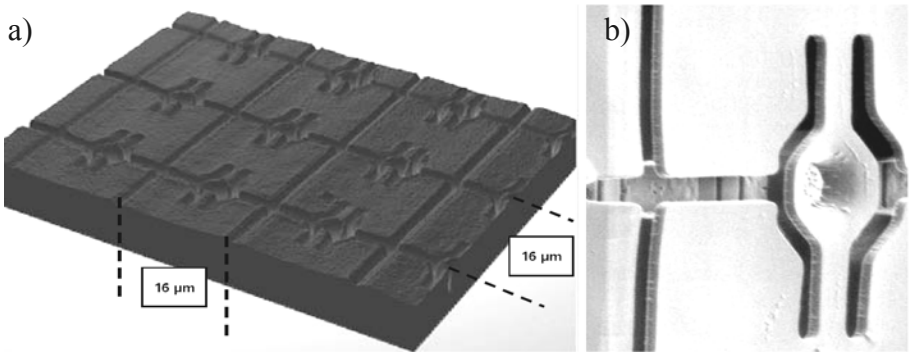

Figure 4.6. a) White light interferometer image of the mirror array; b) a FIB (focused ion beam image of an Al-blade at the hinge section [**Sch**].

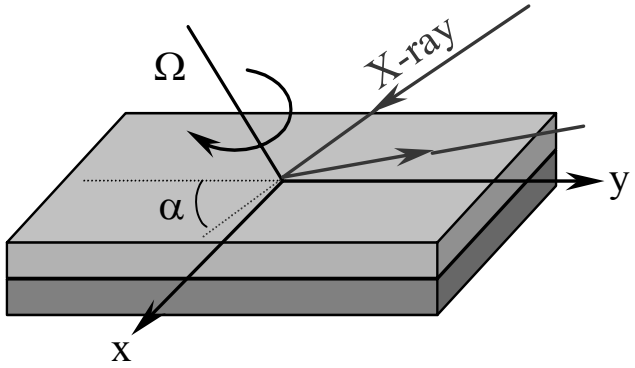

Figure 4.7. Scheme of the omega mode, where the scattering plane is inclined down near to the surface and the shift of the diffraction peak is measured for different ξ-values.

To find residual stress in polycrystalline coatings of good fibre texture the omega mode of the conventional $\sin^2\xi$ technique [**Hauk**] can be applied, its scheme in drawn in **figure 4.7**. According to that the spacing d_{hkl} of the considered lattice plane (hkl) obeys the following relation:

$$(d_{hkl}-d_0)/d_0 \sim \sigma_{xx} \cdot \sin^2(\Delta\Omega)\cdot (1+ \vartheta_{hkl})/E_{hkl}, \qquad (4.1)$$

with σ_{xx} the stress component in x-direction (**Figure 4.6**), d_0 the stress free reference value and $(1+ \vartheta_{hkl})/E_{hkl}$ the corresponding x-ray elastic constants.

4.2.1 Experimental procedure

The investigation of residual stress at a free standing aluminium mirror was carried out using of silicon nanofocusing parabolic refractive x- ray lenses at ID13 (ESRF,

Grenoble). A NFL setup, similar to that of section 3.5, for a photon energy of 15.2 keV was used to generate beam with a lateral size of 180 nm × 100 nm.

To analyse a distribution of residual stresses across an individual mirrors, the samples with different angles of incidence α to the beam direction (**Figure 4.7**) were prepared. The angles of incidence amounted 20, 30, 60, 70, and 80 degrees. To determinate stress on the basis of diffraction peak, each sample was brought in the rotation center and diffraction patterns by different rotation positions were made. The exposure time was 10 s per diffraction.

The diffraction patterns were analysed with the program FIT2D [**FIT2D**], which was calibrated with a corundum (Al_2O_3) standard sample. Note that there are several reflexes in the centre of diffraction pattern (**Figure 4.8**). They are due to higher harmonics in the beam, which scattered from the Pt-pinhole, and are neglected by the sample analysis.

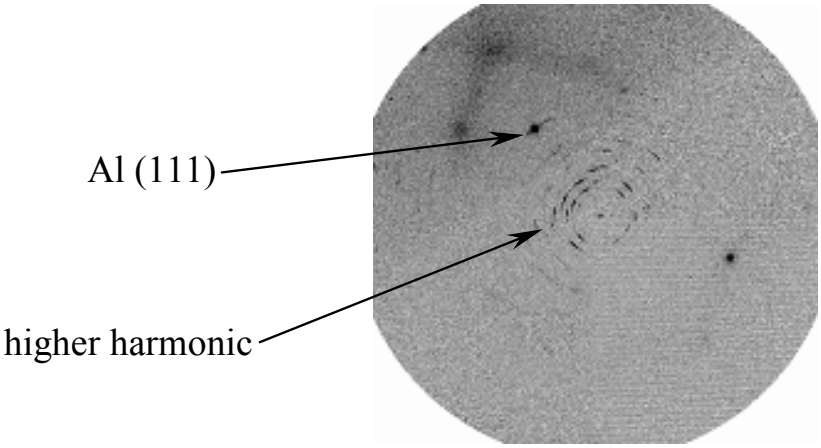

Figure 4.8. Diffraction from the Al-mirror (exposure time 10 s). Reflections in the centre are due to higher harmonics in the beam and are neglected in the sample analysis. Analysis of the residual stress was made by using 111-reflex with the corresponding theoretical value of interplanar spacing of 2.338 Å.

4.2.2 Results

Diffraction from an individual Al-mirror is shown in **figure 4.8**. By using the well visible 111-reflex the interplanar spacing for the different rotation positions (**Figure 4.9a**) and shift of inteplanar spacing in the rocking mode of $\sin^2(\Delta\Omega)$ were determined (**Figure 4.9b**).

For the calculating of residual stresses (**Equation 4.1**), the x-ray elastic constants were taken from the bulk material. Stresses of about 25 MPa were found.

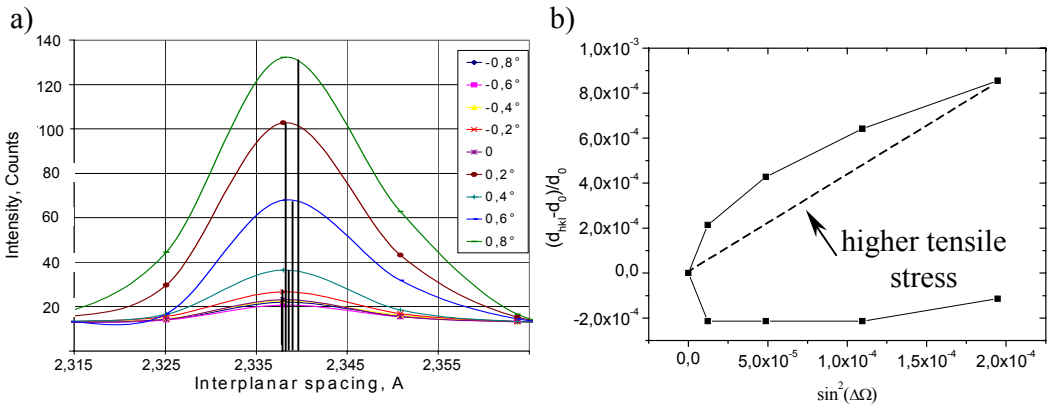

Figure 4.9. a) Interplanar spacing of 111-reflex for the different rotation positions and b) shift of interplanar spacing in the rocking mode of $\sin^2(\Delta\Omega)$.

4.2.3 Discussion and conclusion

To investigate residual stress at individual aluminium mirrors, stress analysis by microfocus x-ray diffraction is required. Using silicon nanofocusing refractive x-ray lenses, a beam of 180 nm × 100 nm for an x-ray energy of 15.2 keV was generated.

The experiment was successful carried out, stress of a free standing aluminium mirror was calculated to be 25 MPa.

Chapter 5

Fabrication of nanofocusing lenses made of boron, diamond, pyrolitic graphite, and sapphire

The well known microfabrication process for silicon makes this material attractive for nanofocusing x-ray refractive lenses. On the other hand, the relatively large atomic number (Z=14) and, as a consequence, the high absorption allow one to reach a diffraction limit below 30 nm only for energies above 20 keV (**Figure 2.9**). Using a weakly absorbing lens material (low atomic number Z), a diffraction limit below 20 nm is already conceivable at 10 keV. However, for low absorbing materials, the numerical aperture is dominated by the geometrical aperture for the lenses with a short focal distance and not by absorption in the outer parts of the lens, which is usually the case for refractive lenses with large focal distance. Therefore, lithium (Z=3), the material with lowest Z which is solid at room temperature, that is often quoted as the best lens material due to its superior ratio σ/μ, is not well suited for this short lens design due to its low density (0.53 g/cm^3) and weak refraction. Moreover, the handling of this material is very difficult due to its strong tendency for oxidation [**Duf**]. The next suitable candidate for the fabrication of the x-ray lenses is beryllium with the atomic number of 4 (**Figure 2.9**). In our group, beryllium lenses with radii of curvature of about 200 mm [**Len1**] have been successfully produced. However, beryllium may cause a health risk when Be powder is generated during the lens

production [**Chem**]. For lenses with rotationally parabolic profile, this risk can be controlled. The next chemical element in the periodic table is boron (Z=5). The ratio of x-ray refraction to absorption for boron is more than 20 times better in comparison to that of silicon. Furthermore, boron has a low level of SAXS and thus is an excellent material for x-ray lenses (**Figure 2.9**) [**Tüm**].The next element is carbon with Z=6. Three modification of carbon are of interest as lens material: diamond, graphite, and glassy carbon. The high density of diamond (3.51 g/cm^3) makes it an interesting candidate for x-ray lenses (**Figure 2.9**), in particular for NFLs. However, it is difficult to transfer the lens profile into a layer of polycrystalline diamond. Pyrolitic graphite (density 2.2 to 2.26 g/cm^3) and glassy carbon density (1.5-2.0 g/cm^3) can be shaped by reactive ion etching. But they have a high level of SAXS. Not only pure elements can be used for NFLs. Sapphire, due to high density and low Z, has low SAXS data and low absorption.

While for boron, diamond, graphite, and sapphire a diffraction limit below 20 nm could be theoretically reached, practically, their microstructuring processes are not developed yet to a point that allows one to reach this limit. In this chapter microfabrication processes of nanofocusing lenses made of materials listed above are discussed, including the main fabrication difficulties and possible strategies to overcome them.

5.1 Boron NFLs

5.1.1 Structure of boron layer

Boron layers produced by chemical vapour deposition (CVD) are not easily available on the market. Specialty Materials, Inc. [**SM1**] - uses a proprietary CVD process to

produce ultra-pure coatings of boron. Layers of 300 μm are deposited on a 3 mm graphite substrate with a purity of 99.999% [**SM2**]. In order to check the crystallographic structure of the boron layer, x-ray diffraction (XRD) was carried out. Details of XRD are outlined in **Appendix I**.

The scan rate of 0.5 °/min was chosen to obtain a good peak–to–background ratio, and 2θ–scans were acquired from 20 to 80°. Scattered x–rays were detected with a θ–resolution of 0.02°. The generator settings were 30 kV and 30 mA, and Cu–Kα radiation was used. The results of the diffraction measurements are presented in a diffractogram (**Figure 5.1**), which shows the intensity of the scattered x–rays as a function of 2θ, which then can be compared to data stored in forms of JCPDS – cards (joint committee on powder diffraction standards). The data obtained from the diffraction experiments have also been used to calculate the interplanar spacing of boron. It is believed that four crystalline modification of boron exist, i.e. α-rhombohedral, α-tetragonal, β-tetragonal, and thermodynamically stable β-rhombohedral phase [**Amb**].

The evaluation of the diffraction measurements has shown, that boron layers used in our experiment has the β-rhombohedral structure (**Figure 5.2**).

5.1.2 Optimisation of the microfabrication process of boron NFLs

The first boron NFLs were developed in our group [**Gat**]. However, several improvements in the microfabrication process are needed. These include the improved adhesion between boron and a mask, an improved etch selectivity between

the mask and boron, an improved mask shape, an increased etch depth of the trenches in boron. SI 591 RIE system from Sentech Instruments was used. The optimized microfabrication process of boron NFLs is described below.

In contrast to silicon wafers, whose surface is very smooth and no subsidiary polishing is needed, the initial surface roughness of the boron layers is more as 20 μm. For microstructuring, however, a surface roughness below 200 nm is desirable. Therefore, the boron layers were polished with polycrystalline diamond paste and diamond suspension of decreasing grain size (from 3 μm to 0.25 μm) for several hours.

Next, the boron samples were cleaned. The cleaning process is very important as it serves to remove any dirt and contamination from the surface of the samples that can

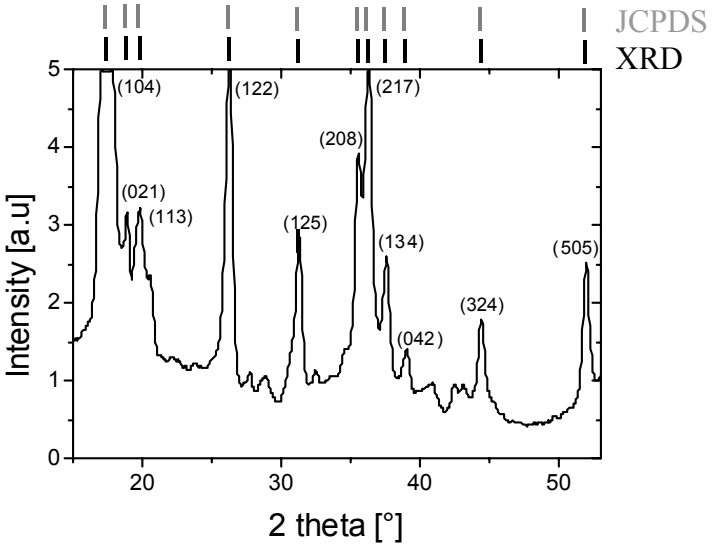

Figure 5.1. Diffractogramm from the boron layers produced by CVD. The calculation shows that it is the β-rhombohedral phase.

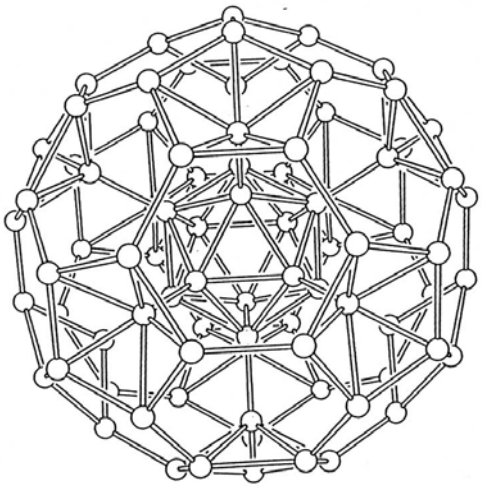

Figure 5.2. The rhombohedral β-boron (R-105) structure.

negatively influence the adhesion of the mask. The samples were immersed in acetone in an ultrasonic bath for ten minutes at a temperature of 60 °C. Then the cleaning process was continued in propanol and dried with a N_2-ion gun. To finally remove organic contaminants such as dust, grease and polishing agent from the surface, the boron layers were etched in a pure oxygen plasma at the gas inflow of 10 sccm, a total pressure of 20 Pa, and rf power of 100 W. The plasma was switched off after 2 min.

By the interaction with oxygen boron is oxidized to boron trioxide (**Equation 5.1**) which is in turn converted to the boric acid by the interaction with water in air (**Equation 5.2**)

$$4B+3O_2 \rightarrow 2B_2O_3, \quad 5.1$$

$$B_2O_3+3H_2O \rightarrow 2H_3BO_3. \quad 5.2$$

The thin liquid boric acid layer (the thickness of 2-3 nm) is removed from the surface by an SF_6 plasma. The etching was done using a gas inflow of 10 sccm, a total **Figure**

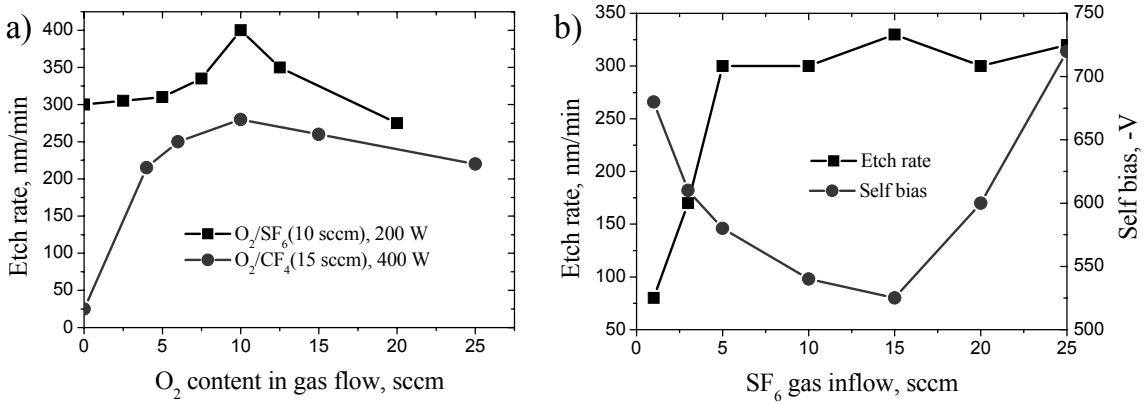

5.3. a) Comparison of boron etch rates for different gas mixtures, where O_2 gas flow was varied. b) Etch rate of boron and self-bias for different gas flow in a pure SF_6 plasma (5 Pa, 200 W).

pressure of 5 Pa, and rf power of 100 W, etching time of 30 s. For better adhesion between boron and the mask, a 3 nm chromium layer was evaporated on the clean boron surface.

Moreover, an etching process for boron based on fluorine gas was developed. As for many other elements, boron is attacked by halogens. While many chemical reactions with boron take place only at elevated temperatures, fluorine reacts already at room temperature. In order to test the etch rate, part of the samples were masked with a Kapton tape. The samples were left in different fluorine containing plasmas for ten minutes. After etching the Kapton tape was removed and the etch depth was measured by means of a surface profilometer.

From silicon technology it is known that the addition of oxygen in a plasma increases the etch rate. **Figure 5.3a** shows the etch rates of boron in a fluorine based plasma with different concentrations of oxygen. The effect of the oxygen in the processing plasma is twofold. On the one hand, the etching rate of boron is increased

(**Figure 5.3a**). On the other hand, the presence of oxygen in the plasma reduces the selectivity of the mask material to boron. Moreover, the etching rate of boron in an SF_6 based plasma (with as well as without oxygen) was found to be higher as compared to CF_4 based plasma. Since the selectivity of the mask material to boron and the etching rate have to be as high as possible, it was decided to use an SF_6 based plasma (high etch rate) without oxygen (high selectivity).

Then the SF_6-based boron etch process was optimised. The etching is primarily chemically driven, and the etch rate is limited by the amount of available reactant (dissociated F). There are a number of ways to increase the F concentration in the reactor: raise the process pressure or increase the total flow of reactants.

Increasing the pressure leads to an increase in the available F-concentration and consequently to an increase in the boron etch rate. In this case, the increased rate typically occurs at the expense of more isotropic profiles and of degraded etch rate uniformity. Also, pressures above 6.5 Pa resulted in tapered edge profiles.

Increasing the total flow is a second way to increase the boron etch rate. At a gas flow above 5 sccm the etch rate was almost independent of the gas feed (**Figure 5.3b**). However, a decreasing self-bias was observed for higher gas flow. Further increasing of the gas flow (above 15 sccm) leads to an increased of self-bias, that is undesirable due to mask erosion. Therefore, a gas flow between 10 and 15 sccm is a good compromise.

Increasing of rf power is a third way to increase the boron etch rate at the expense of increasing the mechanically driven etching. Although the etch rate of boron increases with the rf power, the selectivity in boron/mask material limits the rf power to values below 300 W (**Figure 5.4**).

As an overall result, the best parameters for boron etching were determined to be

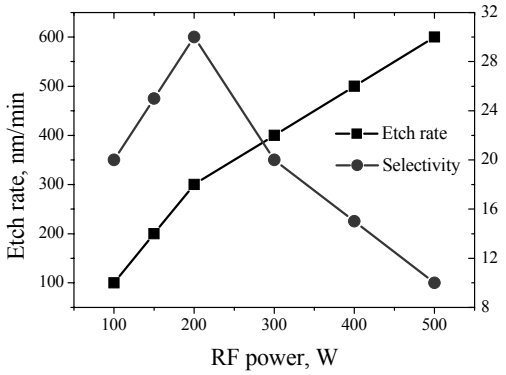

Figure 5.4. Etch rate of boron and etch selectivity of boron to Al-mask as a function of power.

10 sccm SF_6 gas flow at a pressure of 5 Pa, and an rf power of 200 W. For these parameters an etching rate of 300 nm/min was obtained.

At the same time, the choice of mask materials is very important in the boron microfabrication process. From reactive ion etching it is known, that the best mask materials for fluorine based plasmas are chromium and aluminum [**Slo**]. Both materials were tested and it was found that the selectivity of the chromium mask to boron is 1:60 and the selectivity of the aluminum mask to boron is 1:30. It means that etching a 25 μm boron layer requires a 0.8 μm thick Al mask or a 0.4 μm thick Cr mask. Since the structuring of the chromium mask is more difficult, aluminum was chosen as mask material for boron.

To produce NFLs, the polished, cleaned, and chromium coated (3 nm) boron samples were covered with an 1 μm thick aluminum layer. As a mask for the aluminium we have used electron beam evaporated chromium with a thickness of 150 nm. Then the samples were double coated with the positive e-beam resist PMMA 600K using a spin coating system at a rotating speed of 6000 rpm during 30 s. The resist was

annealed at 175 °C for 5 minutes. The coated wafers were structured by e-beam lithography at an exposure dose of 170 μC/cm^2. After EBL processing the samples were developed in the fast e-beam resist developer AP 600-55 for 13 s. The chromium layer of 150 nm was structured in a mixture of ammonium cerium IV-nitrate and perchloric acid (chromium-etch 3144) at room temperature for 2 min corresponding to an etch rate of about 75 nm/min. The end point was detected visually by color changes (from dark metallic for chromium to bright metallic for aluminium). For stopping the etching process the sample was transferred to destilled water at room temperature.

The aluminum etch transfers the pattern in the chromium layer into the aluminum mask. This is done by a dry etching process. Since aluminum is commonly used in microelectronics research, its plasma etch characteristics is well known and chlorine-based chemistry has been widely used for aluminum etching. The etch uses a pure

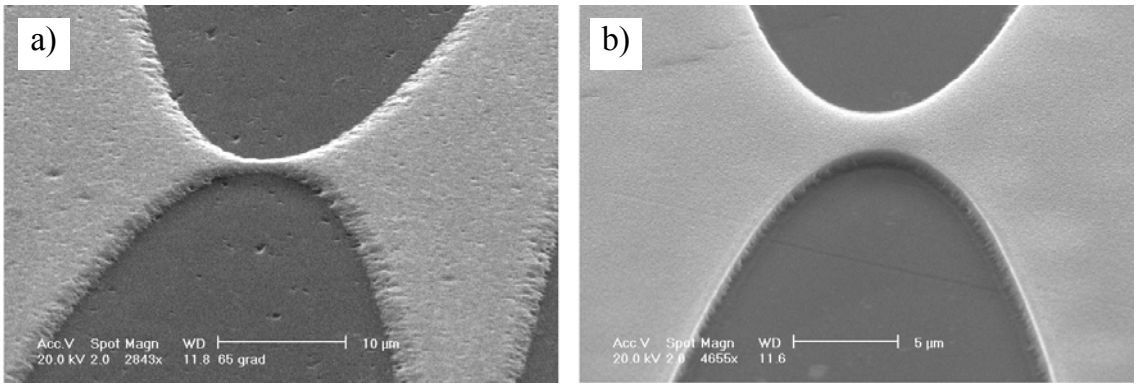

Figure 5.5. a) 1 μm thick aluminium mask structured with wet chemistry shows an isotropic etch profile. b) Dry etching of 1 μm aluminium mask with BCl_3 generates vertical sidewalls.

BCl_3 gas (10 sccm) at a pressure of 5 Pa and an rf power of 200 W. The etch time was 30 min corresponding to an etch rate of 35 nm/min. In comparison to wet etching, dry etching allows to improve the quality of the mask (**Figure 5.5**).

The underlying boron is structured in a reactive ion etching system using pure SF_6 plasma at a gas inflow of 10 sccm, a pressure of a 5 Pa and an rf power of 200 W. To obtain vertical sidewalls, the wafer was cooled by switching off the plasma for 30 s every 30 s. After etching, the wafer was placed in an ultrasonic bath for 30 s to remove RIE grass (**Figure 5.6a**). After a total effective etching time of around 1.5 hour an etch depth of 25 μm was obtained (**Figure 5.6b**).

As in the case of silicon NFLs (**Chapter 3**), in order to provide flexibility concerning the choice of the focal length and of the photon energy, different numbers of single lenses in one NFL and different radii of curvatures are required. The number of single lenses in a boron NFL was 30 and 60. The radius of curvature, R, varies from 2.0 μm

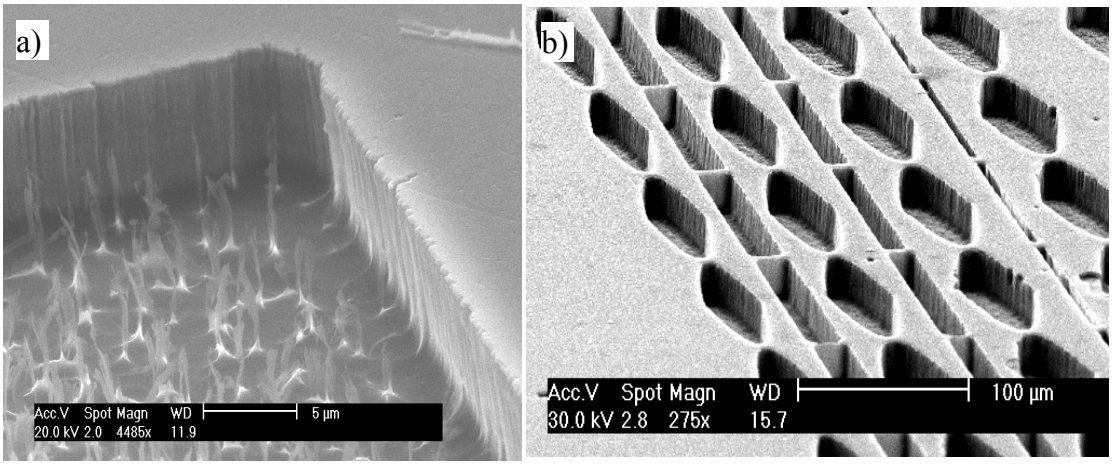

Figure 5.6. Scanning electron micrograph of a) RIE grass by the etching of boron in the SF_6 plasma; b) planar parabolic refractive nanofocusing lenses made of boron.

to 4.0 μm in steps of 0.5 μm, resulting in 5 different NFLs per block. The distance, d, between the apices of a single lens is about 5 μm and the length of a single lens is 145 μm. Different numbers of trenches between two NFLs are used to identity a lens with a given curvature. The mask and the final result of the etching may vary form. Hence, three sets of blocks were written. The mask corrections vary from 0 to 400 nm in steps of 200 nm.

The experiment was performed at 13 keV photon energy, at beamline ID13 of the ESRF in Grenoble, France. The lens system sketched in f**igure 3.9** was mounted at L_1=47 m from the source. The horizontally placed lens (N=60) had a radius of curvature of R=3.0 μm. The vertically placed lens (N=30) had a radius of 4.0 μm. The resolution of the lenses was determined by knife-edge scans with a gold test sample, which is commonly used for this purpose. The FWHM of the line focus of about 2.0 μm was derived from the horizontal fit which is a factor 40 larger than theoretically expected.

The most possible reason conceivable for the observed discrepancy between the theoretical and experimentally determined focal size of a boron lens is the boron surface. The great hardness of boron enables to make the surface smooth but not flat. The consequence of the surface curvature in the range of 10 μm is that not all lenses in one nanofocusing lens can take part in the focusing of x-rays. In this case, the boron lenses can be adjusted so that either some of the first and some of the last lenses in one nanofocusing lens (**Figure 5.7a**) can focus together. Another possibility for the creation of a focus is that an arbitrary fraction of the lenses in an NFL are illuminated (**Figure 5.7b**). The ideal case would be very flat surfaces from the beginning of the microfabrication process as for the silicon lenses (**Figure 5.7c**).

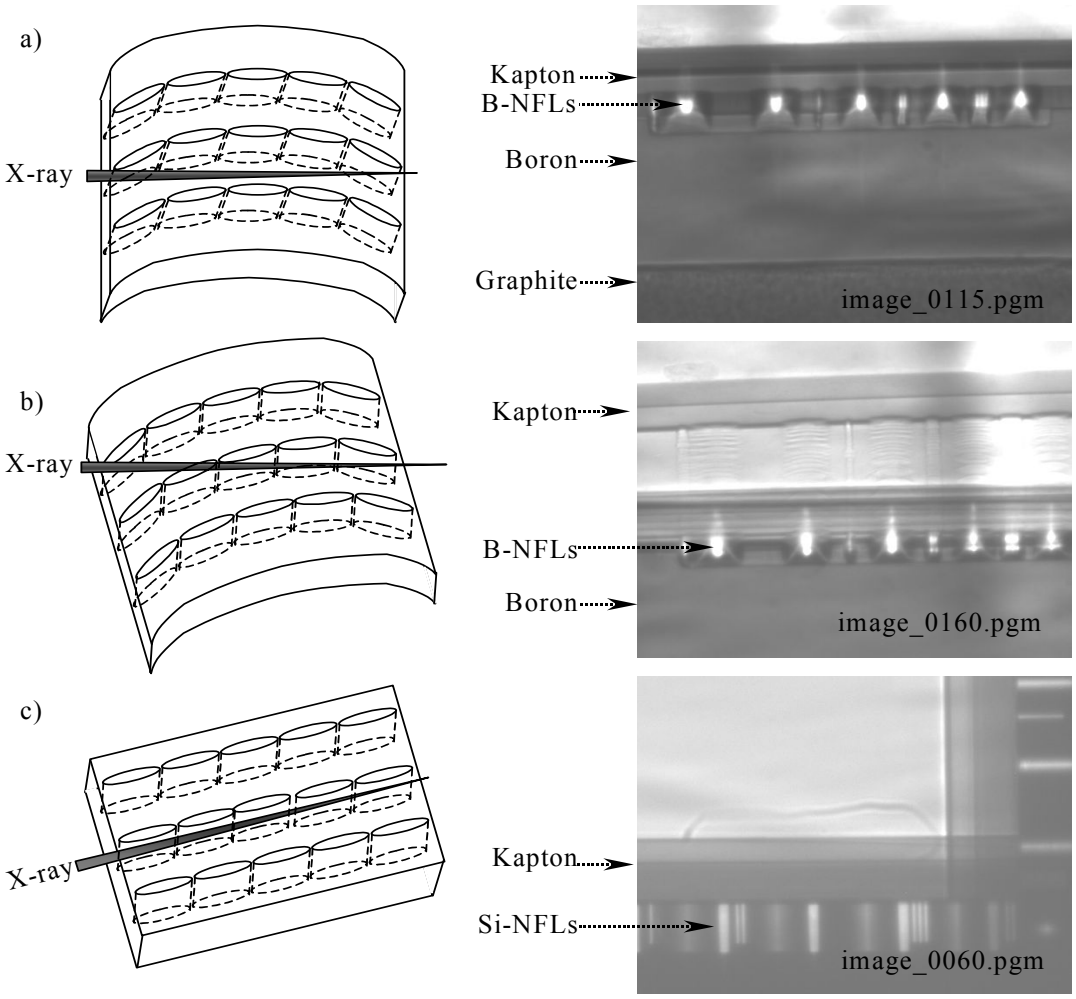

Figure 5.7. Schematic sketches and images of lenses taken in transmission with the high resolution x-ray camera for the different possibilities of the focusing. Due to a curved boron surface only few lenses in one nanofocusing lens (NFL) could be used for the focusing of x-rays. a) Some of the first and some of the last boron lenses in one NFL take part in the focusing. b) Some fraction of the boron lenses in an NFL creates a focus. c) Due to a flat surface from the beginning of the microfabrication process, all silicon lenses in an NFL focus.

In future, using boron layer with the flat surface, lenses with better focusing properties can be obtained.

5.2 Etching of diamond

For the fabrication of diamond nanofocusing lenses we have started with diamond layers, 200 μm thick, which were deposited by chemical vapor deposition (CVD). The films were optically polished to a surface roughness of 15 nm. Reactive ion etching of diamond was done in O_2/CF_4 and in O_2/Ar mixtures. The mask materials were e-beam evaporated Al, Au and Ti as well as CVD deposited Al_2O_3 and AlN.

The highest etching rates of diamond were achieved by using an O_2+CF_4 gas mixture (**Figure 5.8)**. The etching rate of 65 nm/min was obtained at the gas inflow of 40 sccm of O_2 and 6 sccm of CF_4 at the total pressure of 6.5 Pa and at an rf power of 350 W. With a O_2+Ar gas mixture an etching rate of 25 nm/min was achieved at the gas inflow of 40 sccm of O_2 and 10 sccm of Ar at the total pressure of 6.5 Pa and at an rf power of 500 W. The etching rate was found to decrease significantly to 13 nm/min when the gas inflow was changed to 8 sccm of O_2 and 7 sccm of Ar at a pressure of 0.33 Pa and at an rf power of 300 W. A subsequent increasing of the rf power to 400 or 500 W does not lead to increase etching rate.

The selectivity of the etching process was investigated by using Al, Al_2O_3 AlN, Au, SiO_2 and Ti as mask materials. The etching of the Al, Al_2O_3, AlN, Au and SiO_2 masks was realized in an O_2+CF_4 gas mixture with the gas inflow of 40 sccm of O_2 and 6 sccm of CF_4 at the total pressure of 6.5 Pa. The etching experiments were done at an rf power of 100, 250 and 350 W. It was found, that Al has the best selectivity to diamond. The etching rate of Al was 10 nm/min, which corresponds to a selectivity of 6.5. In other words, for etching a diamond layer of 20 μm the mask should be least

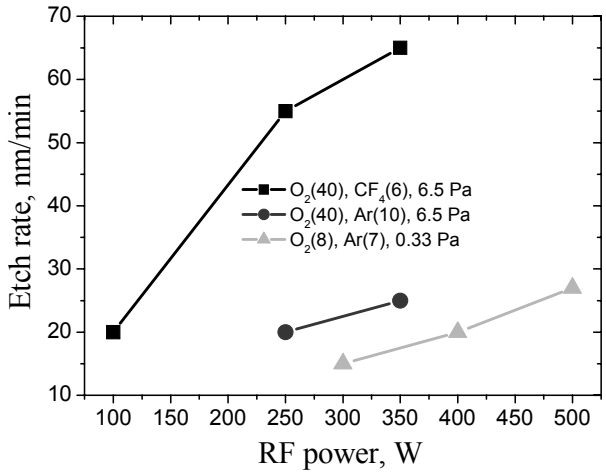

Figure 5.8. Comparison of diamond etching rate for different processing gas mixtures and rf power values.

3.0 μm thick. However, for a mask thickness of several μm the structuring process is difficult to realize.

For the etching in the O_2+Ar gas mixture a better selectivity of the mask material to diamond was obtained by using titanium as mask material. In this case, the etching rate of Ti was found to be 1.4 nm/min at a gas inflow of 40 sccm of O_2 and 10 sccm of Ar, a total pressure of 6.5 Pa and an rf power of 350 W. The etching rate of the Ti mask can be reduced to 0.1 nm/min when the gas inflow was adjusted to 8 sccm of O_2 and 7 sccm Ar at a pressure of 0.33 Pa and an rf power of 400 W. Using the titanium mask with a thickness of 1 μm the diamond can be etched to a depth of 20 μm. Moreover, the mask with a thickness of 1 μm can easily be deposited and structured.

To produce the NFLs the polycrystalline diamond films were coated with a 300 nm thick titanium layer. As mask material for titanium an aluminum layer with a

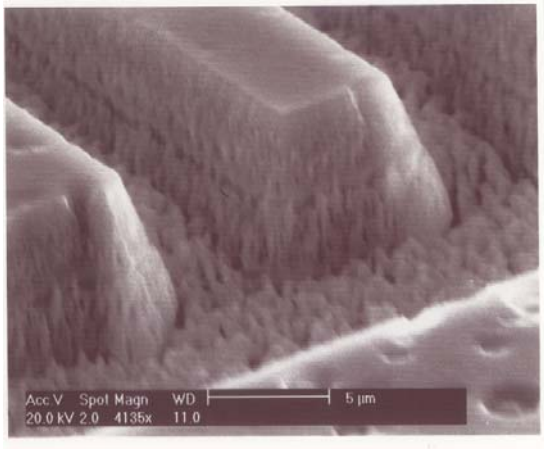

Figure 5.9. SEM image of an etched diamond sample. Etch parameters: 8 sccm of O_2 and 7 sccm of Ar, total pressure of 0.33 Pa, rf power of 500 W. Etching time is 6 hours.

thickness of 200 nm was used. The samples were then covered with the positive e-beam resist AR 7400.23 using a spin coating system where the wafer is rotated at 4000 rpm for 30 s. the resist was annealed at 85 C for 1 minute. The coated wafers were structured by EBL at an exposure dose of 180 μC/cm^2 and then treated in the developer AR 300-47 for 65 s. The aluminum was etched by RIE using pure BCl_3. An etching rate of 35 nm/min was achieved at a gas inflow of 10 sccm, a total pressure of 5 Pa and at an rf power of 200 W. An etching rate of 60 nm/min for titanium was obtained by using SF_6 as a processing gas with inflow rate of 5 sccm, a total pressure of 5 Pa and at an rf power of 200 W. Finally, the diamond was etched in an O_2+Ar gas mixture at a pressure of 0.33 Pa and at an rf power of 500 W. After an etch time of 6 hours a depth of about 6 μm was achieved (**Figure 5.9**). Due to the low etching rate and the destruction of the mask at the edges, the underlying diamond structures show heavily tilted sidewalls. The present result of diamond shaping is completely

inadequate for nanofocusing x-ray lenses. Better etching procedures have to be developed, maybe along the line proposed in [**Enl**].

5.3 Pyrolitic graphite NFLs

Glassy carbon was not considered as lens materials due to its extremely high amount of SAXS. On the other hand, pyrolitic graphite with a density above 2.2 g/cm^3 was tested as lens materials. Ideal graphite has a density of 2.26 g/cm^3. The difference in density accounts for SAXS still present in pyrolitic graphite. In this material, layers of graphite are ordered along the c-axis, the orientation of the sheets in the ab-plane is random [**Pie**].

It is well known that graphite can be etched in an O_2-plasma and the best mask material is titanium due to a good selectivity to graphite [**Slo**]. The microfabrication of the graphite NFLs was optimized by varying the total pressure, the rf power and the gas inflow. A selectivity value of about 65 was obtained by etching in the O_2 plasma at the total pressure of 2 Pa and at an rf power of 500 W. In addition, it was found that introducing argon resulted in a decreased etching rate (**Figure 5.10a**).

After the etching parameters were established, the production of the NFLs was done according to the following scheme. The pyrolitic graphite samples were polished with diamond paste. The polished samples were covered with a 400 nm thick titanium layer deposited by e-beam evaporation. Then they were coated with e-beam resist AR 7400.23. The next steps were a structuring with EBL at an exposure dose of 190 μC/cm^2 and the development in AR 300-47 for 65 s. The titanium layer was structured in a BCl_3 plasma at a gas inflow of 10 sccm, total pressure of 5 Pa, and rf power of 200 W. After structuring the titanium layer, the graphite was etched in the oxygen plasma at the gas inflow of 35 sccm, a total pressure of 5 Pa, and rf power

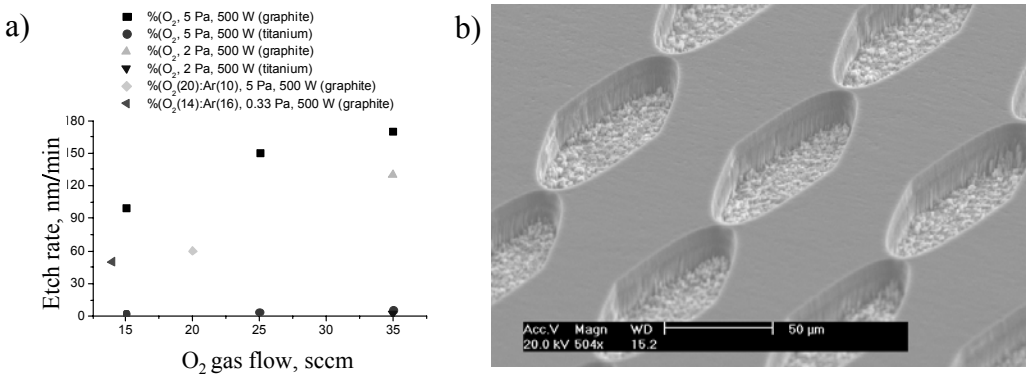

Figure 5.10. a) Comparison of pyrolitic graphite and titanium etch rates for different gas mixture. O_2 gas flow was varied. b) Scanning electron micrograph of an array of parabolic refractive x-ray lenses made of pyrolitic graphite (N=60, R=2-4 μm, l=8.6 mm).

of 200 W. The plasma was switched off for 10 min every 10 min to allow cooling of the wafer. During the cooling time the sample was taken out from the RIE chamber and dipped in an acetone ultrasonic bath for 3 min to remove RIE grass and then cleaned in propanol and dried in a nitrogen stream. Then the wafer was placed again into the RIE system. After a total effective etch time of around 4 hours an etch depth of 25 μm was achieved (**Figure 5.10b)**.

The lenses were tested at ID13 of ESRF in Grenoble, France. The synchrotron radiation was monochromatised to 15.22 keV. The lenses were mounted at a distance of 47 m from the source. The beam was horizontally focused with 60 lenses. The lenses tested have a radius of curvature of 3 μm. The integral flux behind the lens was measured to $F_0=2.2\times10^9$ ph/s. Using the graphite lenses a focal size of 2 μm was obtained. This measured value is much bigger than the calculated focal size of 50 nm [**NFL**]. Possible reason for this discrepancy could be:

1) The sidewalls (tilt around 3-5 degrees) were not vertical, thus destroying the focusing properties of the graphite NFLs.
2) SAXS, due to the voids responsible for the reduced density, generates a strong blur of the focal spot.

5.4 Etching of sapphire

Sapphire is a very hard aluminium oxide, single crystalline, non-porous, unaffected by weathering and hydration, its density is 3.98 g/cm^3. These and other properties offer many advantages to the optical designer. In the last years, optical components including windows, lenses and mirrors made of sapphire have been fabricated. Due to a small atomic number, and as consequence, to a weak absorption and low level of SAXS data, sapphire is an attractive material for nanofocusing refractive x-ray lenses. It has been reported that it is difficult to etch Al_2O_3 films because of its high chemical and physical stability. In contrast to silicon (**Chapter 3**), the etching process of sapphire has not been developed, so far. High sapphire etch rates with high etch selectivity over mask materials are required. Recently, research on the various etching of sapphire such as ion beam etching [**Hay**], chemical wet etching after ion implantation [**Don**], reactive ion etching [**Fed**], [**Kim**], laser-assisted etching and inductively coupled plasma [**Sung**] have been carried out.

In order to test the application of RIE for fabrication of nanofocusing lenses made of sapphire, several etch experiments were carried out. The highest etching rates of sapphire were achieved using pure BCl_3. The etching rate of 25 nm/min was obtained at the gas inflow of 20 sccm, at the total pressure of 2 Pa and at an rf power of 590 W. The etching rate was found to decrease significantly to 13 nm/min when the gas

inflow was changed to 10 sccm. With a pure SF_6 gas an etching rate of 10 nm/min was achieved at the gas inflow of 25 sccm, at the total pressure of 2 Pa and at an rf power of 500 W. Due to these low etching rates structures in sapphire with vertical sidewalls and a depth over 20 μm can be not obtained. Based on the experimental results it is proposed that the significant improvement of the etching rate can be obtained by using ICP etching system [**Sam**].

Chapter 6

Summary and outlook

In this research, an optimised deep reactive ion etching process for the fabrication of refractive lenses with a cylindrically parabolic profile made of silicon is presented. As compared to the first silicon NFLs [**Schr1**], the contact between sample and reactive ion etching (RIE) chamber was improved. As a consequence, steeper sidewalls were obtained. Deep silicon etching was applied using a thin silicon dioxide mask. Due to the high selectivity between silicon and silicon dioxide (about 300) a lens depth of 62 μm was obtained. Based on the results of the shape analysis, the lenses with the best parabolic profile and vertical sidewalls were selected for the experiments. As a result of the significantly improved lens shape, the lateral resolution achieved with these lenses approaches the theoretical limit. The silicon lenses described in this work are very useful optical components for nanofluorescence tomography, nanodiffraction and other techniques done at third generation synchrotron radiation sources.

In a recent experiment made at the European Synchrotron Radiation Facility (ESRF) in Grenoble, France, these lenses were used to generate a nanobeam of 47 nm × 55 nm for an x-ray energy of 21 keV [**Schr6**]. The performance of the silicon lenses was proved in several application oriented experiments.

Silicon nanofocusing refractive x-ray lenses make possible an analysis of the structural transformations in thin films of phase change media. The illuminated volume was reduced to 180 nm × 100 nm × 80 nm, which corresponds to ~10^7 atoms. In general, more diffraction patterns should be made for a reliable analysis of the

experimental data. In future, nanofocusing x-ray lenses may allow for the investigation of the time dependence of the crystallization process and for the influence of the temperature – time variation in the laser modified areas.

To investigate residual stress at individual aluminium mirrors, stress analysis by microfocus x-ray diffraction is required. Using silicon nanofocusing refractive x-ray lenses, a beam of 180 nm × 100 nm for an x-ray energy of 15.2 keV was generated. The experiment was successfully carried out, stress of a free standing aluminium mirror was calculated to be 25 Mpa.

To achieve a lateral focal size under 20 nm nanofocusing refractive x-ray lenses made of diamond, graphite, sapphire or boron are required. Up to now, microfabrication processes for these elements are not well developed. Using a RIE system from Sentech, the microfabrication process of boron NFLs was optimised. This includes the improved adhesion between boron and a mask, an improved etch selectivity between the mask and boron, an improved mask shape, an increased etch depth of the trenches in boron. Further improving of the roughness of boron layers, i.e. the smoothness and the flatness is expected to lead to boron nanofocusing lenses with focusing properties approaching the theoretical value.

To develop a mictofabrication process for diamond, a RIE system was used. Different gas mixtures and mask materials were investigated to find the highest etch rate of diamond and the maximum selectivity of diamond to the mask material. The best mask material for diamond was found to be titanium with a selectivity of about 20. Using an O_2+Ar gas mixture an etch rate of 1 μm/hour was achieved. Due to the low etching rate, the underlying diamond structures show heavily tilted sidewalls, that make them completely inadequate for nanofocusing x-ray lenses. Using a modern etching

equipment, i.e. an inductively coupled plasma (ICP) system, better diamond shaping can be obtained.

To produce nanofocusing refractive lenses made of pyrolitic graphite, an etching procedure similar to that for diamond etching was developed. Using a pure oxygen plasma an etch rate of up to 6.5 μm/hour was obtained. Relatively high etch rates make it possible to control the tilt of the sidewalls. The lenses were tested at ID13 of ESRF in Grenoble, France. A focal size of 2 μm was obtained. This measured value is much bigger than the calculated focal size of 50 nm [**NFL**]. A possible reason for this discrepancy could be scattering, which generates a strong blur of the focal spot, due to the voids responsible for the reduced density.

Furthermore, some experiments of sapphire etching were performed in order to test the applicability of a RIE system for production of sapphire nanofocusing lenses. Etching rate of 25 nm/min was found. Due to this low etching rate in sapphire no vertical sidewalls could be obtained. Based on the experimental results it is proposed that a significant improvement of the etching rate can be obtained by using ICP etching system.

According to the results of this work the following conclusions can be made:

- The microfabrication process of silicon nanofocusing lenses is optimised. With these lenses a lateral resolution of 50 nm was achieved and this resolution approaches the theoretical limit. Using the same process for the fabrication of silicon adiabatically focusing lenses (AFL), described in **section 2.10**, a lateral resolution of 20 nm and below can be reached.
- Silicon nanofocusing refractive x-ray lenses are useful optical components for nanofluorescence tomography, nanodiffraction and other techniques done at third generation synchrotron radiation sources. Using these lenses, the

analysis of structural transformations in thin films of phase change media and the investigation of residual stress in aluminium mirrors were made. In future, fluorescence tomography experiments with a resolution in the range of 100 nm are feasible.

- To fabricate nanofocusing x-ray lenses made of boron, sapphire or diamond, improved microfabrication techniques are required. In the case of boron, a polishing machine is needed, which allows the boron surface to be smooth and flat, simultaneously. For the etching of sapphire and diamond, a ICP etching system is required. Using such a system, vertical sidewalls of the etched structures may be at hand.

Appendix I.
X–ray diffraction (XRD)

X–ray diffraction is a non–destructive analytical technique for the identification and quantitative determination of various crystalline forms.

When a polycrystalline (powder) sample is irradiated with monochromatic x–rays, in addition to absorption and other phenomena, elastic x–ray scattering may occur. The intensity and angular distribution of the scattered x–rays from a crystalline sample allow one to determine the lattice structure and the position of the atoms in the unit cell. Bragg's law defines where reflections can be expected:

$$n\lambda = 2d\sin\theta, \qquad (1)$$

where λ is the wavelength, d is the distance between the atomic planes in the crystal, and θ is the Bragg angle at which a diffraction peak is observed.

The results of the diffraction measurements are presented in a diffractogram, which shows the intensity of the scattered x–rays as a function of 2θ, which then can be compared to data stored in forms of JCPDS (joint committee on powder diffraction standards) – cards. The data obtained from the diffraction experiments can also be used to calculate the interplanar spacing of the sample.

X–ray diffraction using conventional Bragg–Brentano geometry is only partially suitable for the analysis of the thin films due to the unfavorable peak–to–background ratio. A grazing incidence attachment is designed for the measurements of thin films, surfaces and multilayers. Applying small incidence angles (0.1 to 3°) of the x–ray beam leads to strongly reduced penetration depths and an increased size of the irradiation area. Soller slits help to define the direction of the incoming and diffracted

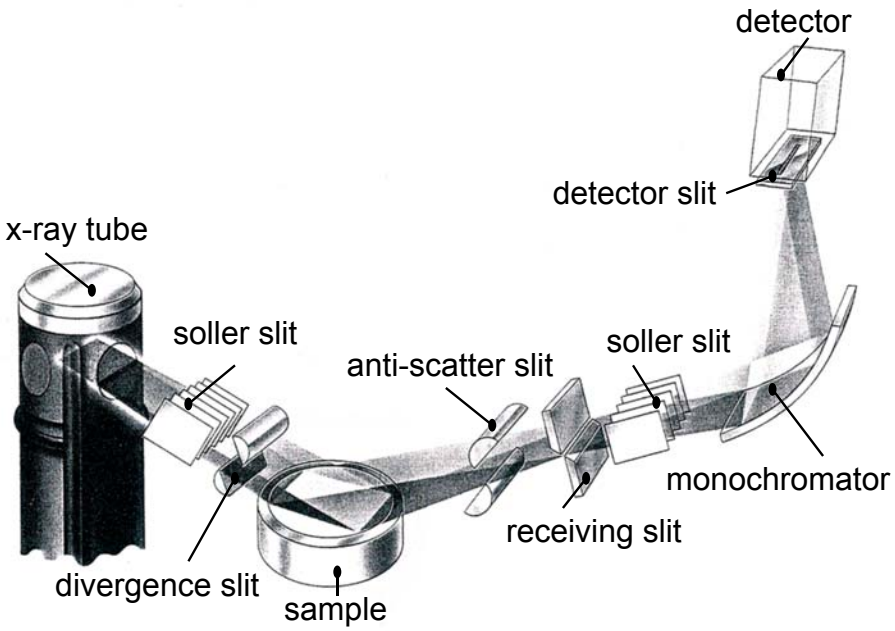

Figure 1. Schematic representation of the diffractometer

beams (Figure 1).

The crystallographic structure and the texture of the deposited boron films were determined by x–ray diffraction (XRD) with a Siemens D500 diffractometer, which was operated at a grazing incidence angle of 3°. The scan rate of 0.5 °/min was chosen to obtain a good peak–to–background ratio, and 2θ–scans were acquired from 20 to 80°. Scattered x–rays were detected with a θ–resolution of 0.02°. The generator settings were 30 kV and 30 mA , and Cu–Kα radiation was used. The diffractometer was calibrated with a polycrystalline Si sample.

List of Figures

List of Tables

Bibliography

[Amb] E. Amberger, K. Ploog, *J. Less. Common. Met.*, **23**, p.21, 1971.

[And] E. H. Anderson, D. L. Olynick, B. Harteneck, E. Veklerov, G. Denbeaux, W. Chao, A. Lucero, L. Johnson, D. Attwood, *J. Vac. Sci. Technol. B*, **18**(6), 2970, 2000.

[Aris] V. Aristov, M. Grigoriev, S. Kuznecov, L. Shabelnikov, V. Zunkin, T. Weitkamp, C. Rau, I. Snigireva, A. Snigirev, M. Hoffmann, E. Voges, *Appl. Phys. Lett*., **77**, 4058 (2000).

[Ayón] A. A. Ayón, R. L. Bayt, K. S. Breuer, *Smart Mater. and Struct.*, **10**, 1135, 2001.

[Ber] C. Bergemann, H. Keymeulen, and J. F. van der Veen, *Phys. Rev. Lett*., **91** (20), 204801, 2003.

[Berg] M. Berger, J. Hubbell, S. Seltzer, J. S. Coursey, and D. S. Zucker, *XCOM: Photon Cross Section Database,* http://physics.nist.gov/PhysRefData/Xcom/html/xcom1.html.

[Boer] M. J. de Boer, et al, *J. Microelectromech. Sys.*, **11**, 385, 2002.

[Chem] *"Chemical Bachgrounder"*, http://www.nsc.org/library/chemical/.

[Chab] M. Chabloz, Y. Sakai, T. Matsuura, K. Tsutsumi, *Microsys. Technol.*, **6**, 86, 2000.

[Chan] C. Y. Chang, S. M. Sze, *ULSI Technology. The McGRAW-Hill Companies Inc,* 1996.

[Cloe] P. Cloetens, O. Hignette, S. Bohic, E. Pereiro, C. Ch. Morawe, W. Ludwig, *SRI 2003, San Francisco, 25-29 August*, online presentation, see http://www.sri2003.lbl.gov/html/presentations.thml.

[Clou] R. L. Clough, *Nucl. Instr. and Meth. B*, **185**, 8, 2001.

[Dav] C. David, B. Kaulich, R. Medenwaldt, M. Hettwer, N. Fay, M. Diehl, J. Thieme, G. Schmahl, *J. Vac. Sci. and Technol. B*, **13**(6), 2762, 1995.

[Don] X. Dongzhu, Z. Dehang, P. Haochang, X. Hngjie, R. Zongxin, *J. Appl. Phys.*, **31**, 1647, 1998.

[Duf] E.M. Dufrence, D. A. Arms, R. Clarke, N. R. Pereira, S. B. Dierker, D. Foster, *Appl. Phys. Lett.*, **79**(25), 4085, 2001.

[Enl] J. Enlund, *"ICP Etching of Single Crystal HTHP and CVD Diamond"*, February, 2003.

[Fed] J. B. Fedison, T. P. Chow, H. Lu, I. B. Bhat, *J. Electrochem. Soc.*, **144**, 221, 1997.

[FIT2D] http://www.esrf.fr/computing/scientific/FIT2D/.

[Fri1] I. Friedrich, V. Weidenhof, W. Njoroge, P. Franz, M. Wuttig, *J. Appl. Phys.,* **87**, 4130, 2000.

[Fri2] I. Friedrich, V. Weidenhof, S. Lenk, M. Wuttig, *Thin Solid Films*, **389**, 239, 2001.

[Gat] M. Gather, Bachelors thesis: *„Boron nanofocusing refractive x-ray lenses"*, Aachen, 2004.

[Grig] I.S. Grigoriev, E. Z. Meilikhov, *„Handbook of physical Quantities"*, **CRC Press**, Boca Raton, New York, London, Tokyo, 1997.

[Hauk] V. Hauk, H. Behnken, W. Reimers, W. Pfeiffer, Ch. Genzel, *"Structural and Residual Stress Analysis by Nondestructive Methods"*, Elsevier Health Sciences, 1997.

[Hay] A. Hayes, J. F. Welden, E. Ostun, R. J. Gambino, *Data Storage 43* (March/April), 1995.

[Haya] S. Hayakawa, N. Ikuta, M. Suzuki, M Wakatsuki, T. Hirokawa, *J. Syn. Rad.*, **8**, 328, 2001.

[Hech] E. Hecht and A. Zajac, *"Optics"*, Addison-Wesley Publishing Company, 2nd edition, 1987.

[Hign1] O Hignette, G. Rostaing, P. Cloetens, A. Rommeveaux, W. Ludwig, A. Freund, *in "X-ray Micro- and Nano- Focusing: Applications and Techniques II"* (ed. by McNulty), SPIE 4499, San Diego, 105, 2001.

[Hign2] O. Hignette, P. Cloetens, W. K. Lee, W. Ludwig, G. O. Rostaing, *Journal de Physique IV*, **104**, 231, 2003.

[Hop] J. Hopkins, et al, *MRS Symposiom Proceedings*, **vol. 546**, 63, Boston 1998.

[Ice] G. E. Ice, J. Chung, J. Z. Tischler, A. Lunt L. Assoufid, *Rev. Scient. Inst.*, **71**(7), 2635, 2000.

[Ich] M. Ichinose, T.Ishida, Y. Takagai, M. Ito, S. Ohara, I. Satoh, Y. Okazaki, R. Imanaka, *Jpn J. Appl. Phys.*, **32**, 5320, 1993.

[Jam] R. W. James, *"The optical principles of the diffraction of x-rays,"* Cornell University Press, 1967.

[Kim] J. W. Kim, Y. C. Kim, W. J. Lee, *J. Appl. Phys.*, **78**, 2045, 1995.

[Kirk] P. Kirkpatrick, A.V. Baez, *J. Opt. Soc. Am.*, **38**, 766, 1948.

[Köhl] M. Köhler, *„Etching in Microsystem Technology“*, **WILEY-VCH Verlag GmbH**, 1999.

[Len1] B. Lengeler, C. G. Schroer, M. Richwin, J. Tümmler, M. Drakopoulos, A. Snigirev, I. Snigireva, *Appl. Phys. Lett.*, **74** (26), 3924, 1999.

[Len2] B. Lengeler, C. G. Schroer, B. Benner, A. Gerhardus, T. F. Günzler, M. Kuhlmann, J. Meyer, C. Zimprich, *J. Syn. Rad.*, **9**, 119, 2002.

[Len3] B. Lengeler, J. Tümmler, A. Snigirev, I. Snigireva, C. Raven, *J. Appl. Phys*, **84** (11), 5855, 1998.

[Len4] B. Lengeler, C. Schroer, M. Kuhlmann, B. Benner, T. Günzler, O. Kurapova, F. Zontone, A. Snigirev, I. Snigireva, *J. Phys. D: Appl. Phys.,* **38**, 1, 2005.

[Liu] H.-C. Liu, Y.-H. Lin, W. Hsu, *Microsys. Technol.*, **10**, 29, 2003.

[Mich] A. G. Michette, *“Optical systems for soft x-rays”*, Plenum Press, New York, 1986.

[NFL] Calculating, using the software NFLCALC which was developed by C. G. Schroer, www.xray-lens.de.

[Pie] H. O. Pierson, *“Handbook of carbon, graphite, diamond and fullers”*, 1993.

[Prot] V. V. Protopopov, K. A. Valiev, *Opt. Commun*., **151**, 297, 1998.

[Rai] P. Rai-Choudhury, *“Microlithography, Micromachining and Microfabrication”*, volume 1. SPIE Optical Engineering Press, 1997.

[Sam] www.samcointl.com/apps/mems.html.

[Sch] J. Schreiber, S. Braun, A Gatto, H. Schenk, *Proceeding of SPIE*, **5392**, 18, 2004.

[Schr1] C. G. Schroer, M. Kuhlmann, U. T. Hunger, T. F. Günzler, O. Kurapova, S. Feste, F. Frehse, B. Lengeler, M. Drakopoulos, A. Somogyi, A. S. Simionovici, A. Snigirev, I. Snigireva, C. Schug, W. H. Schröder, *Appl. Phys. Lett.*, **82** (9), 1485, 2003.

[Schr2] C. G. Schroer, B. Lengeler, *Phys. Rev. Lett.*, **94**, 054802, 2005.

[Schr3] C. G. Schroer, *„Hard x-ray microscopy and microanalysis with refractive x-ray lenses“*, RWTH Aachen University, Department of Physics, habilitation, 2004.

[Schr4] C. G. Schroer, M. Kuhlmann, O. Kurapova, T. Hunger, T. Günzler, S. Feste, B. Lengeler, S. Ziegler, M. Drakopoulos, M. Burghammer, C. Riekel, A. Snigirev, I. Snigireva, "*Design and Microfabrication of Novel X-ray Optics II", Proceedings of SPIE*, **5535**, 10, 2004.

[Schr5] C. G. Schroer, T. Günzler, M Kuhlmann, O. Kurapova, S. Feste, M. Schweizer, B. Lengeler, W. Schröder, M. Drakopoulos, A. Somogyi, A. Simionovici, A. Snigirev, I. Snigireva, "*Developments in X-ray Tomography IV", Proceeding of SPIE*, **5535**, 162, 2004.

[Schr6] C. G. Schroer, O. Kurapova, J. Patommel, P. Boye, J. Feldkamp, B. Lengeler, L. Vincze, A. van der Hart, M. Küchler, *Appl. Phys. Lett.*, 2005.

[Schn] G. Schneider, T. Schliebe, H. Aschoff, *J. Vac. Sci. Technol. B*, **13**(6), 2809, 1995.

[Shin] M. Shinotsuka, T. Shibaguchi, M. Abe, Y. Ide, *Jpn. J. Appl. Phys*., **36**, 536, 1997.

[Slo] D. Slovetsky, *"Mechanism of the materials etching in plasma",* Lections.

[SM1] Specialty Materials, Inc., 1449 Middlesex Street, Lowell, MA, USA, http://www.specmaterials.com.

[SM2] Data provided by Specialty Materials Inc.

[Snig] A. Snigirev, V. Kohn, I. Snigireva, B. Lengeler, *Nature*, **384**, 49, 1996.

[Spec] S. J. Spector, C. J. Jacobsen, D. M. Tennant, *J. Vac. Sci. Technol. B*, **15**(6), 2872, 1997.

[Sung] Y. J. Sung, H. S. Kim, Y. H. Lee, J. W. Lee, S. H. Chae, Y. J. Park, G. Y. Yeom, *Mat. Sci. and Engin. B82*, 50, 2001.

[Tam] N. Tamura, R. S. Celestre, A. A. MacDowell, H. A. Padmore, R. Spolenak, B. C. Valek, N. Meier Chang, A. Manceau, J. P. Patel, *Rev. Sci. Instr.*, **73**(3), 1369, 2002.

[Tüm] J. Tümmler, *"Development of Compound Refractive Lenses for Hard X-Rays"*, Dissertation RWTH Aachen, **Shaker Verlag**, 17, 2000.

[Veig] W. J. Veigele, *"Mass attenuation and absorption cross section for 94 elements; 0.1 keV to 1 MeV"*, in "Handbook of Spectroscopy", ed. by J. W. Robinson, **CRC Press**, Inc., Bosa Raton, Florida 33431, USA, 28, 1980.

[Vol] B. Volland, et al, *J. Vac. Sci. and Techn. B*, **17**, 2768, 1999.

[Yam] K. Yamauchi, K. Yamamura, H. Mimura, Y. Sano, A. Saito, A. Suvorov, M. Yabashi, K. Tamasaku, T. Ishikava, Y. Mori, *J. Syn. Rad.*, **9**, 313, 2002.

[Yama] N. Yamada, E. Ohno, N. Akahira, K. Nishiuchi, K. Nagata, M. Takao, *Jpn. J. Appl. Phys.*, **26**, 61, 1987.

[Yun] W. Yun, B. Lai, Z. Cai, J. Maser, D. Legnini, E. Gluskin, Z. Chen, A. Krasnoperova, Y. Vladimirsky. R. Cerrina, E. Di Fabrizio, M. Gentili, *Rev. Sci. Instr.*, **70**(5), 2238, 1999.

Acknowledgements

PhD project always comes to fruition only with the assistance of many people. Here I would like to thank all who contributed directly (and indirectly) to the quality of this work:

- Prof. Dr. B. Lengeler for the very interesting topic and efficient supervision on all stages of my thesis,
- Prof. Dr. U. Klemradt for agreeing to act as co-referee in this work,
- Dr. Schroer who introduced the world of x-ray optics and of article writing to me and whose enthusiasm and optimism always was helpful,
- Dr. T. Hunger who introduced the microfabrication techniques to me and always helped with many tips and tricks of RIE and not only,
- all members of our group – B. Benner, P. Boye, J. Feldkamp, S. Feste, F. Frehse, F. Günzler, M. Kuhlmann, J. Patommel, M. Schweitzer, C. Zimprich - for the warm atmosphere and fruitful discussions, what ever a subject was and letting me keep my experimental work in a good form. People, who were always ready to give me a small lecture about right German and local dialect, respectively.
- our secretaries - R. Weinkauf, A. Schüren and S. Vurgun – for help with the office work and office techniques, for sweets and tee, for smiles and countenance,
- to all people of mechanical workshop of the University, to P. Kordt and W. Retetzki in particular, who were very patient to realized all technical ideas for the lens setup,

- K. D. Schaefer from the electrical workshop for reanimating the low-voltage voltmeter for galvanic and D. Schulte, especially, for his help with the cooling system for the evaporation plant,
- ESRF people - I. Snigireva, A. Snigirev, M. Drakopoulos, M. Burghammer, C. Riekel, F. Zontone, A. Somogyi, A. Simionovici - for the friendly and communicative atmosphere, without their help our experiments would be not so successful,
- FZ - Jülich people - A. Steffen for the careful evaporation of Si-wafer and for possibility to use modern rein room in my aims, A. van der Hart for e-beam lithography over a long period of time and for an unceasing interest to results of the experiments, W. Schröder for interesting discussion about biological objects,
- ZfM people, especially M. Küchler, for professional etching our Si lenses and for care during my visit in Chemnitz,

- The very special thanks is addressed to my husband Denis for his support, understanding, believe and everything else.

Curriculum Vitae

Personal details:

Name	Olga Kurapova
Maiden name	Prokopenko
Date of birth	03.04.1977
Place of birth	Tashkent, USSR
Marital status	married, no children
Nationality	Russian

School education:

09/1984-06/1994	Secondary school with profound study of Physics and Math, Tashkent, USSR

University education:

09/1994-06/1998	Bachelor's degree in Physics of Condensed Matter, Moscow State Steel and Alloys University, Department of Physical Chemistry
09/1998-06/2000	Master's degree in Physics of Condensed Matter, Moscow State Steel and Alloys University, Department of Theoretical Physics
04/2002-10/2005	Ph. D. student at the II. Physicalisches Institut B, RWTH, Aachen University